NASA/TP-2001-210398

Thermostructural Analysis of Unconventional Wing Structures of a Hyper-X Hypersonic Flight Research Vehicle for the Mach 7 Mission

William L. Ko and Leslie Gong
NASA Dryden Flight Research Center
Edwards, California

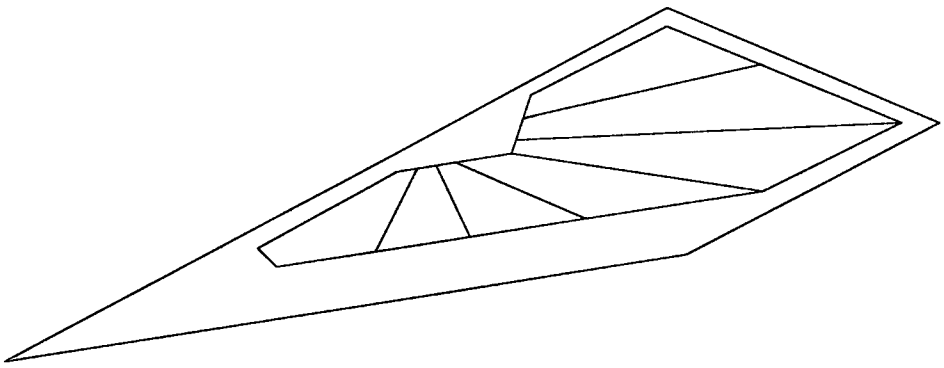

October 2001

The NASA STI Program Office...in Profile

Since its founding, NASA has been dedicated to the advancement of aeronautics and space science. The NASA Scientific and Technical Information (STI) Program Office plays a key part in helping NASA maintain this important role.

The NASA STI Program Office is operated by Langley Research Center, the lead center for NASA's scientific and technical information. The NASA STI Program Office provides access to the NASA STI Database, the largest collection of aeronautical and space science STI in the world. The Program Office is also NASA's institutional mechanism for disseminating the results of its research and development activities. These results are published by NASA in the NASA STI Report Series, which includes the following report types:

- TECHNICAL PUBLICATION. Reports of completed research or a major significant phase of research that present the results of NASA programs and include extensive data or theoretical analysis. Includes compilations of significant scientific and technical data and information deemed to be of continuing reference value. NASA's counterpart of peer-reviewed formal professional papers but has less stringent limitations on manuscript length and extent of graphic presentations.

- TECHNICAL MEMORANDUM. Scientific and technical findings that are preliminary or of specialized interest, e.g., quick release reports, working papers, and bibliographies that contain minimal annotation. Does not contain extensive analysis.

- CONTRACTOR REPORT. Scientific and technical findings by NASA-sponsored contractors and grantees.

- CONFERENCE PUBLICATION. Collected papers from scientific and technical conferences, symposia, seminars, or other meetings sponsored or cosponsored by NASA.

- SPECIAL PUBLICATION. Scientific, technical, or historical information from NASA programs, projects, and mission, often concerned with subjects having substantial public interest.

- TECHNICAL TRANSLATION. English-language translations of foreign scientific and technical material pertinent to NASA's mission.

Specialized services that complement the STI Program Office's diverse offerings include creating custom thesauri, building customized databases, organizing and publishing research results...even providing videos.

For more information about the NASA STI Program Office, see the following:

- Access the NASA STI Program Home Page at ***http://www.sti.nasa.gov***

- E-mail your question via the Internet to help@sti.nasa.gov

- Fax your question to the NASA Access Help Desk at (301) 621-0134

- Telephone the NASA Access Help Desk at (301) 621-0390

- Write to:
  NASA Access Help Desk
  NASA Center for AeroSpace Information
  7121 Standard Drive
  Hanover, MD 21076-1320

NASA/TP-2001-210398

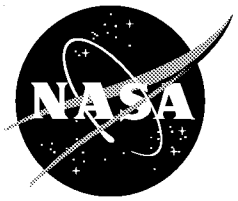

Thermostructural Analysis of Unconventional Wing Structures of a Hyper-X Hypersonic Flight Research Vehicle for the Mach 7 Mission

William L. Ko and Leslie Gong
NASA Dryden Flight Research Center
Edwards, California

National Aeronautics and
Space Administration

Dryden Flight Research Center
Edwards, California 93523-0273

October 2001

NOTICE

Use of trade names or names of manufacturers in this document does not constitute an official endorsement of such products or manufacturers, either expressed or implied, by the National Aeronautics and Space Administration.

Available from the following:

NASA Center for AeroSpace Information (CASI)
7121 Standard Drive
Hanover, MD 21076-1320
(301) 621-0390

National Technical Information Service (NTIS)
5285 Port Royal Road
Springfield, VA 22161-2171
(703) 487-4650

ABSTRACT

Heat transfer, thermal stresses, and thermal buckling analyses were performed on the unconventional wing structures of a Hyper-X hypersonic flight research vehicle (designated as X-43) subjected to nominal Mach 7 aerodynamic heating. A wing midspan cross section was selected for the heat transfer and thermal stress analyses. Thermal buckling analysis was performed on three regions of the wing skin (lower or upper); 1) a fore wing panel, 2) an aft wing panel, and 3) a unit panel at the middle of the aft wing panel. A fourth thermal buckling analysis was performed on a midspan wing segment. The unit panel region is identified as the potential thermal buckling initiation zone. Therefore, thermal buckling analysis of the Hyper-X wing panels could be reduced to the thermal buckling analysis of that unit panel. "Buckling temperature magnification factors" were established. Structural temperature-time histories are presented. The results show that the concerns of shear failure at wing and spar welded sites, and of thermal buckling of Hyper-X wing panels, may not arise under Mach 7 conditions.

NOMENCLATURE

a	length of rectangular plate, in.
b	width of rectangular plate, in.
CL	clamped boundary condition
c_p	specific heat, Btu/lb-°F
E	Young's modulus, lb/in^2
E23	two-nodes bar element
E33	triangular combined membrane and bending element
E43	quadrilateral combined membrane and bending element
FR	panel edge supports allowing free in-plane motion (free)
FX	panel edge supports with no in-plane motion (fixed)
JLOC	joint location (node)
k	thermal conductivity, Btu/hr-ft-°F
LTA	Lockheed Thermal Analyzer
SPAR	Structured Performance and Resizing
SS	simply supported boundary condition
T	temperature, °F
T_{mat}	average temperature for material properties, °F
T_n	temperature at node n
T_o	peak temperature of dome-shaped temperature distribution, °F
T_s	panel boundary heat sink temperature, °F
T_u	uniform temperature distribution, °F

TPATH	Dryden computer simulation program
TPS	thermal protection system
t	time counted from the air-launching of Pegasus booster rocket from B-52, sec.
VIEW	computer program to compute view factors, see equation (1)
$( )_{cr}$	critical buckling value at buckling
α	coefficient of thermal expansion, in/in-°F
ε	emissivity
η	$= (T_o)_{cr}/(T_u)_{cr}$, *Buckling temperature magnification factor of the first kind* = buckling temperature $(T_o)_{cr}$ of dome-shaped temperature loading (fixed or free support condition) divided by the buckling temperature $(T_u)_{cr}$ of uniform temperature loading (fixed support condition).
λ_c	eigenvalue associated with uniform temperature loading
λ_o	eigenvalue associated with dome-shaped temperature loading
ν	Poisson's ratio
ξ	$= (T_o)_{cr}/(T_o)_{cr}\mid_{T_s = 0}$ *Buckling temperature magnification factor of the second kind* = buckling temperature $(T_o)_{cr}$ of dome-shaped temperature loading case with any heat sink temperature $T_s \neq 0$ (free support condition) divided by the buckling temperature $(T_o)_{cr}$ of dome-shaped temperature loading case with zero heat sink temperature $T_s = 0$ (free support condition)
ρ	density, lb/in^3
σ_f	uniaxial tensile failure stress, lb/in^2
σ_T	ultimate tensile strength, lb/in^2
σ_x	chord-wise stress, lb/in^2
σ_Y	yield strength, lb/in^2
τ_f	sheer failure stress, lb/in^2
τ_{max}	maximum shear stress, lb/in^2

INTRODUCTION

Hypersonic flight vehicles are subjected to severe aerodynamic heating during flights. To maintain structural integrity at these high temperatures, the vehicle structural design concepts for high Mach number vehicles are different from those of low Mach number aircraft. The vehicle structure may be called "hot" structures or "warm" structures, depending on the operating temperature range. The hot structures are fabricated with high-temperature materials and are capable of operating at elevated temperatures exceeding 1000 °F. Typical hot structural components are carbon/carbon composite

structures, hat-stiffened panels fabricated with either monolithic titanium alloys or metal-matrix composite materials, and honeycomb sandwich panels fabricated with high-temperature materials such as Titanium, or nickel-based Inconel® (Inco Alloys International, Inc., Huntington, West Virginia) alloys. The warm structures are fabricated with light-weight materials such as aluminum and must be insulated so that the sub-structural temperatures will not exceed the operating temperature limit of 350 °F. The space shuttle orbiter is a good example of warm structure. The entire vehicle is protected with a thermal protection system (TPS) to shield the aluminum substructure from overheating beyond the warm temperature limit (ref. 1).

An example of a recent hot structure is the new hypersonic flight research vehicle called Hyper-X (designated as the X-43 vehicle), which has unconventional wing structures with irregular-shaped wing panels (described in the following section).

Temperature distributions in the hot structures are, in general, not uniform because of cooler substructures such as spars and ribs. The nonuniformity of the structural temperature distribution induces thermal stresses. Excess thermal stresses could cause vehicle wing panels to buckle and creep, and could also cause the skin and spar weld sites to lose bonding integrity. A uniform temperature field induces no thermal stresses in structures fabricated with materials that have the same coefficient of thermal expansion. Thermal buckling problems are of great concern for both hot and warm structures, and have been extensively studied by Ko (refs. 2-11). Those past thermal buckling studies were conducted on rectangular-shaped honeycomb sandwich and hat-stiffened panels, and not on irregular-shaped panels such as the Hyper-X wing panels.

To fully understand the thermostructural performance of the unconventional Hyper-X wing structures under nominal Mach 7 aerodynamic heating*, heat transfer analysis, thermal stress analysis, and thermal buckling analysis must be performed. This requires complex three-dimensional modeling of the Hyper-X wing structures. However, without going through complex modeling of the entire wing structure, one can use a simple method to quickly approximate the panel buckling temperatures of wing panels. This report presents the results of heat transfer analysis and thermal buckling analysis of wing structures using such an approximation method, and discusses how the Hyper-X wing structures would perform under nominal Mach 7 heating.

Use of trade names or names of manufacturers in this document does not constitute an official endorsement of such products or manufacturers, either expressed or implied, by the National Aeronautics and Space Administration.

HYPER-X FLIGHT RESEARCH VEHICLE

Hyper-X (designated as X-43) is a new hypersonic flight research vehicle (12 ft long, 5 ft span, 3,000 lb weight), designed to be flown at a range of Mach 7~10 (fig. 1). The underside of the vehicle consists of an inlet ramp, a scramjet (supersonic-combustion ramjet) engine module, and an expansion ramp. The scramjet engine is an air-breathing ramjet engine in which the airflow through the whole engine remains supersonic. The Hyper-X scramjet engine uses hydrogen as fuel and inlet air as oxidizer (no oxidizer is carried on board). The proposed flight trajectory of Hyper-X is shown in figure 2. The Hyper-X rides on a winged Pegasus booster rocket, which is carried under the wing of a B-52 aircraft up

*It should be noted that the maximum Mach number reached during the nominal Mach 7 mission was 7.5.

to a launch altitude of 17,000 ft. for the Mach 7 mission or 43,000 ft for the Mach 10 mission. After air launching from the B-52, the Pegasus booster rocket will accelerate and ascend to an altitude of approximately 100,000 ft, reaching the test velocity (of Mach 7 or Mach 10). After separation from the booster rocket, the cowl door of the Hyper-X scramjet engine opens to test the performance of the scramjet engine. Once the cowl door is open, fuel is injected, ignited and burned for about 8 seconds. The entire event from the opening to the closing of the cowl door lasts for 34 seconds.

The Hyper-X wing structure is fabricated with high-temperature Haynes 230 alloy (a nickel-chromium-tungsten-molybdenum alloy) which has relatively low thermal expansion characteristics. The design concept of its wing structures (fig. 3) is entirely different from that of the conventional wing structures. The conventional spar and rib system is replaced with multiple radial stiffeners (spars, 0.25 in. wide) fanning out from the pivoting wing roots. To house the instrumentation inside the wing structure, upper and lower wing skins (0.090 inches thick) are divided into two separate wing panels (a fore wing panel and an aft wing panel). The wing panels are then butt-welded at their edges to the main wing frame, and line-welded to the radial reinforcing stiffeners without using conventional fastening screws or rivets. Because the edges of the heated wing panels are constrained, potential thermal buckling of the wing panels and possible shearing off of the line-welded sites are of great concern.

DESCRIPTION OF PROBLEM

Heat transfer and thermal stress analyses are to be performed on the midspan segment of the Hyper-X wing (fig.3). A nominal Mach 7 aerodynamic heating is to be used as heat input to calculate time histories of structural temperatures. The worst-case non-uniform temperature distribution obtained from the heat transfer analysis is to be used for temperature loads to calculate thermal stresses in the wing segment.

Thermal buckling analysis is to be performed on the following three regions of the wing skin panels (lower or upper): 1) the fore wing panel, 2) the aft wing panel, and 3) a unit panel at the middle of the aft wing panel (fig. 3). In addition, thermal buckling is also to be conducted for the wing segment (fig 3). These analyses are being done to locate the thermal buckling initiation zone.

The unit panel is used to establish *buckling temperature magnification factors* (1) to scale up the buckling solution of uniform temperature loading for generating a buckling solution for dome-shaped temperature loading; or (2) to scale up the buckling solution of dome-shaped temperature loading with unheated boundary heat sinks for generating a buckling solution for the same case when the heat sinks are heated up.

HEAT TRANSFER ANALYSIS

The finite-difference heat transfer analyses of Hyper-X wing structures are performed using the Lockheed Thermal Analyzer (LTA). The LTA is a generalized FORTRAN program that computes transient temperature distributions in complex structures based on an electrical analogy of capacitors and resistors.

Finite-Difference Thermal Modeling

The Hyper-X wing segment selected for the heat transfer analysis is located at the wing midspan, approximately 4.7 in. from the wing root edge (fig. 3). The chord-wise region lies between the stream-wise distances 11.0 in. and 18.0 in. measured from the carbon/carbon leading edge, and spans over three neighboring radial stiffeners (or spars) (fig. 3).

Two finite-difference thermal models (fig. 4) were generated for two cases of welded site skin and spar contacts; 1) full contact, and 2) partial contact (inset of fig. 4). The two thermal models are identical (fig. 4) except for the contact resistance between the skin panels and radial stiffeners. Each model consists of 64 capacitors modeling Haynes® 230® (Haynes International, Kokomo, Indiana) alloy. Outer structural mold lines use a 1.5 degree half-angle for both upper and lower skins. For the full contact, the wing skin panels are perfectly bonded to the full width (0.25 in.) of the stiffeners. For the partial contact, the welded site is 0.040 in. wide and 0.01 in. thick. The resistance between capacitors {1 and 66}, {13 and 70}, {25 and 75}, {69 and 41}, {74 and 53}, and {79 and 65} (fig. 4) were calculated for 1) full contact conductance, or 2) partial contact conductance representing a 0.040-inch-width contact area. The partial contact case is a more realistic representation of the actual skin and spar welded sites. The thermal models have a surface emissivity of $\varepsilon = 0.85$. The external radiation view factors were calculated by hand, but the internal radiation view factors were calculated from the VIEW program (described below). The input thermal properties of Haynes 230 alloy are listed in Table A-1 of the Appendix.

Internal Radiation View Factors

The internal radiation view factors were calculated from the VIEW program, which is incorporated into the Structural Performance And Resizing (SPAR) finite-element computer program (ref. 12). Figure 5 shows the two SPAR finite-element radiation models generated for the internal view factor computations. Each model has 63 internal radiation elements. Each of the radiation elements matches the interior surface of each corresponding element of the finite-difference thermal model (fig. 4).

In the computations of internal radiation view factors using the VIEW program, two cases were used: the combined case and the separate case. For the combined case, the entire wing segment was considered as a single enclosure with obstruction at the middle spar (fig. 5-a). For the separate case, each bay was considered independently as an enclosure without obstructions (fig. 5-b).

For case one, the radiation element numbering was started from bay 1 and continued on bay 2, (not independently numbered for each bay). The command OBSTRUCT was used to define the obstructing surfaces, which are the two sides of the middle spar (i. e., elements 12, 13, 14, 15, 16, 59, 60, 61, 62, 63) (fig. 5-a). The ENCLOSURE command was used to identify the system of radiation surfaces as an enclosure, and to correct the calculated view factors so that the sum of the view factors from each radiation element is equal to unity. Namely, if F_{ij} $(i, j = 1, 2, 3, \ldots)$ is the radiation view factor defined as the fraction of radiant heat, leaving radiation element i and incident on radiation element j, then the ENCLOSURE command will enforce the following condition for the final values of F_{ij}.

$$\sum_j F_{ij} = 1 \tag{1}$$

where the summation is taken over j for each given i.

For case two, the internal radiation view factors were computed independently for each bay using the VIEW command. For this case, the radiation elements are numbered independently (starting from No. 1) for each bay (fig. 5-b). Because there is no obstruction within each bay, the ENCLOSURE and UNOBSTRUCT commands were used. The command OBSTRUCT was not needed. The above two approaches (fig. 5-a, 5-b) gave identical internal view factor solutions, thus verifying the accuracy of view factor calculations.

Heating Profile

Figure 6 shows the preliminary flight trajectory for the Mach 7 mission of the Pegasus booster rocket carrying the Hyper-X vehicle. The maximum Mach number of the flight trajectory turned out to be 7.5 (fig.6-c). This was the flight trajectory available at the time of this analysis and was, therefore, used to calculate the aerodynamic heating rates. The Dryden in-house computer code called TPATH was used for these calculations. Various parameters for inputs to the TPATH code are: time histories of altitude, angle of attack, and Mach number (fig. 6) as well as the outer mold-line geometry of the wing cross section. The program calculates transient heating rates and surface temperatures, and also computes heat transfer coefficients, boundary layer recovery temperatures and other parameters required to calculate the aerodynamic heating rates. The program permits the use of different theories for calculating the heat transfer coefficients. These theories can be properly applied at each location of interest for laminar or turbulent flow condition, or for flows with transition. The transition condition can be input as a function of Reynolds number and local Mach number, or prescribed at a specific time. In the present analysis, the transition criteria used resulted in turbulent flow calculations for the entire flight profile. Local flow conditions were calculated for an attached flow using the oblique shock theory (ref. 13). Heat transfer coefficients were calculated using Eckert's *reference enthalphy* method (refs. 14, 15). Calculations were made for the upper and lower surface of the horizontal wing. Real gas properties of air were used in all calculations (ref. 16). Heat transfer coefficients and recovery temperatures calculated from the TPATH code were then used as inputs to the LTA. This thermal analyzer program then calculated the heating rates and corresponding structural temperatures for the two-dimensional thermal models.

THERMAL STRESS ANALYSIS

The SPAR finite-element computer program (ref. 12) is used in the linear thermal stress analysis of the wing segment. The following sections discuss finite element modeling, boundary constraints, and temperature load.

Finite Element Modeling

The wing segment selected for the thermal stress and thermal buckling analysis is located at the wing midspan cross section where the heat transfer analysis is performed (fig. 3). The wing segment has a unit span-wise width, and spans over three neighboring radial stiffeners (spars) in stream-wise direction. The finite-element structural model generated for the wing segment is shown in figure 7. The wing panels and the spars are modeled with a single row of quadrilateral combined membrane and bending elements (E43 elements). The nodal coordinates of the finite-element structural model are made coincidental with those of the finite-difference thermal model (fig. 4). Thus, the nodal temperature output from the thermal model

can be used directly as temperature input to the structural model. Only one welded site at the top of the middle spar (radial stiffener) is modeled in detail for shear stress calculations (inset of figure 7). The wing skin and spar welded site is modeled with E43 elements whose lower boundaries are connected to the middle spar (E43) element through triangular membrane and bending elements (E33 elements). To simulate the effect of stream-wise thermal expansion restraint resulting from the cooler wing frame, the nodes of the three radial stiffeners are interconnected with two nodes (E23 bar elements). The size of the finite-element structural model for the wing segment is listed in Table 1.

Table 1. Number of joint locations and elements of wing-segment finite-element model.

Item	Number
JLOC	166
E23 elements	20
E33 elements	8
E43 elements	95

The temperature-dependent material properties of Haynes 230 used for input to the structural model are listed in the Appendix.

Boundary Constraints

The wing-segment model is allowed to expand freely in all directions. The span-wise edges of the wing panels are constrained to have zero slopes in the span-wise direction to simulate the effect of continuity to neighboring regions.

Temperature Load

The structural temperature distribution at time t = 89 sec (from launch of the Pegasus booster) obtained from the heat transfer analysis is used as thermal load input for the thermal stress analysis. Time t = 89 sec is the instant when the difference between the upper and lower skin peak temperatures reaches a maximum. As will be seen later, this structural temperature distribution over each bay is arch-shaped.

THERMAL BUCKLING ANALYSIS

The SPAR program is also used for the linear thermal buckling analysis of the wing panels. The following sections discuss material property iterations, finite element modeling, boundary conditions, temperature load, and buckling temperature.

Material Property Iterations

In thermal buckling analysis, when high accuracy buckling solutions are sought, the *material property iteration* process is required. This iteration process is described in great detail in ref. 17. Initially, the buckling temperature is still unknown and, therefore, the material properties at a certain assumed temperature (usually room temperature) are first used as input. Once the first-iteration buckling temperature is calculated, the material properties corresponding to the first calculated buckling temperature are input to the second iteration of eigenvalue calculations. This material iteration process (updating material properties) must continue until the temperature used for the input material properties converges with the final buckling temperature. In the present buckling study, the material iteration process (averaging $5 \sim 7$ iterations) for each case was terminated when the assumed material temperature approached the calculated buckling temperature with less than 0.5 percent error.

Finite Element Modeling

The wing-segment model (fig. 7) is also used for thermal buckling analysis. Figure 8 shows the three finite-element models (called the *fore panel model*, the *aft panel model*, and the *unit panel model*) generated respectively for the fore wing panel, aft wing panel, and the unit panel located at the middle of the aft wing panel (fig. 3). All the wing panels are modeled with E43 elements. The boundary heat sinks and radial stiffeners are modeled with E23 bar elements. The sizes of these three wing finite-element models are listed below.

Table 2. Number of joint locations and elements of wing-panel finite-element models.

	Fore panel model	Aft panel model	Unit panel model
JLOC	3116	2419	984
E23 elements	350	276	126
E43 elements	3000	2320	920

Boundary Conditions

Different support conditions listed below are considered for comparative studies of how the buckling temperatures change with the support conditions.

Table 3. Definition of support conditions.

	Panel Boundaries	Panel and Stiffener Welded Sites
SS-SS	simply supported	simply supported
SS-CL	simply supported	clamped
CL-SS	clamped	simply supported
CL-CL	clamped	clamped

Based on the fact that the Hyper-X wing panels (fig. 4-b) are line-welded, the SS-SS condition listed in Table 3 could be the closest to the actual support condition of the Hyper-X wing panels.

Temperature Load

The thermal load inputs used are uniform temperature loading and dome-shaped (or arch-shaped) temperature loading.

Uniform Temperature Loading

Because the actual temperature distributions over the entire wing surfaces are not available, uniform temperature loading will be analyzed first. Figure 9(a) shows an example of a typical uniform temperature loading case for the unit panel. The uniform nodal temperature input is chosen to be $T = T_u = 1°\mathrm{F}$. The eigenvalue λ_c (scaling factor) calculated from the SPAR program will then give the buckling temperature $(T_u)_{cr}$. Namely,

$$(T_u)_{cr} = \lambda_c \times 1°\mathrm{F} \tag{2}$$

This buckling solution is for the uniform temperature loading over the wing panels with fixed supports, and is not the actual case. This buckling solution is the simplest fundamental case, and can show the location of the weakest bay, where thermal buckling is likely to take place. When the panel boundaries can have free in-plane motion (free supports), the uniform temperature loading case obviously can not induce thermal buckling.

Dome-Shaped Temperature Loading

Hot structural panels are usually fastened to the cooler substructures (of relatively large mass) that function as heat sinks. Thus, even under a uniform surface heat flux, the temperature distribution over the

hot panels will not be uniform, but dome-shaped (ref. 18). This is the typical behavior of hot structural panels.

For the wing segment, the calculated dome-shaped temperature distribution obtained from the wing-segment heat transfer analysis is used as the temperature load input.

For the two-dimensional wing panels, temperature distribution over the wing surface must be calculated from heat transfer analysis by the modeling of one complete wing structure. In order to avoid that complexity, the following quick approximation method will be used.

Because the cooler spars function as heat sinks, the calculated temperature distribution over each bay is expected to be dome-shaped based on past hot structural experiments (ref. 18). By observation (fig. 3), the unit panel that has the largest area compared with other sub-panels must be the weakest sub-panel in resisting thermal buckling. Therefore, buckling analysis of the entire wing panels under actual temperature loading can then be reduced to the analysis of the unit panel that is under dome-shaped temperature loading to obtain approximate buckling solutions.

As will be seen shortly, the stream-wise distribution of panel temperature over each bay exhibits an arch-shaped curve (a cross sectional shape of a *dome* surface) because of the existence of heat sinks (cooler radial stiffeners). Such an arch-shaped curve is very similar to part of the *sine* curve. Therefore, for the two-dimensional case, dome-shaped temperature distribution could be a good approximation of the actual surface temperature distribution over any unit panel that is supported by boundary heat sinks.

For a rectangular plate with length a and width b, the dome-shaped temperature distribution (with peak temperature T_o and boundary heat sink temperature T_s) may be ideally described by the following equation.

$$T(x,y) = T_s + (T_o - T_s)\sin\frac{\pi x}{a}\sin\frac{\pi y}{b} \tag{3}$$

which gives a sine × sine surface lifted by an amount T_s.

Equation (3) may be applied directly to the *irregular-shaped* unit panel by simply distorting the boundaries and mesh of the finite-element model generated for the rectangular plate to form the irregular boundaries and mesh of the unit panel model. Thus, the nodal temperatures $T(x,y)$ calculated from equation (3), will automatically provide the nodal temperatures for the unit panel model. Figure 9(b) shows the dome-shaped temperature loading over the unit panel calculated from equation (3). For the Hyper-X case, the ratio of averaged heat sink temperature T_s to the wing panel maximum temperature T_o is roughly $T_s/T_o = 0.54$ at time $t = 89$ sec.

For the dome-shaped temperature load input to the SPAR program for the eigenvalue calculations, the peak temperature $T_o = 1°\text{F}$ was used. The heat sink temperature T_s was allowed to vary over the range $T_s/T_o = 0 \sim 1$ (i.e., $T_s/T_o = 0$, 0.1, 0.2, 0.3, 0.4, 0.5, 0.54, 0.6, 0.7, 0.8, 0.9, 1.0; with $T_s/T_o = 0.54$ being the Hyper-X case). The buckling temperature $(T_o)_{cr}$ for the dome-shaped temperature loading case is then obtained from

$$(T_o)_{cr} = \lambda_o \times 1°\text{F} \tag{4}$$

where λ_o is the eigenvalue calculated from the SPAR program for the dome-shaped temperature loading case. The reason for using the whole range of $T_s/T_o = 0 \sim 1$ is to study the effect of the heat sink temperature T_s on the panel buckling temperature $(T_o)_{cr}$. Keep in mind that the panel buckling temperature $(T_o)_{cr}$ will increase with the increasing heat sink temperature T_s as a result of relaxation of the thermal expansion constraint exerted on the unit panel by the boundary heat sink.

Buckling Temperature Magnification Factors

As will be seen shortly, the buckling temperature $(T_o)_{cr}$ for the dome-shaped temperature loading case is much higher than the buckling temperature $(T_u)_{cr}$ of the uniform temperature loading case (with fixed supports). Therefore, a *buckling temperature magnification factor of the first kind* η defined below

$$\eta = \frac{(T_o)_{cr}}{(T_u)_{cr}} \tag{5}$$

will be used to indicate how many times the buckling temperature $(T_o)_{cr}$ of the dome-shaped temperature loading case (free or fixed supports) is magnified from the buckling temperature $(T_c)_{cr}$ of the uniform temperature loading case with fixed supports (fundamental case).

In reality, the wing panel attempts to expand under heating, but its expansion is resisted by the cooler boundary substructures (heat sinks) which expand less. This boundary constraint is the cause of thermal buckling of the wing panels. Such substructure constraints will gradually relax as the substructures are heated up, resulting in a higher panel buckling temperature. In order to find out how the heat sink temperature T_s affects the panel buckling temperature $(T_o)_{cr}$ for the dome-shaped temperature loading case with free supports, another *buckling temperature magnification factor of the second kind* ξ defined below

$$\xi = \frac{(T_o)_{cr}}{(T_o)_{cr}\big|_{T_s = 0}} \tag{6}$$

will be used to indicate how many times the buckling temperature $(T_o)_{cr}$ for the dome-shaped temperature loading case with free support (SS or CL) is magnified when the heat sink temperature T_s increases from $T_s = 0$ (no heat sink thermal expansion) to a certain non-zero value $T_s \neq 0$ (with heat sink thermal expansion).

RESULTS

The results of the heat transfer analysis, thermal stress analysis, and thermal buckling analysis of the Hyper-X wing structure subjected to Mach 7.5 heating (the nominal Mach 7 mission) are presented in the following sections.

Heat Transfer

Figure 10 shows the time histories of nodal temperatures $\{T_{13}(t), T_{70}(t)\}$ at nodes {13, 70} of the middle spar upper welded site (fig. 4) for the full and partial contact cases. The nodal temperature difference $(T_{13} - T_{70})$ is slightly higher for the partial contact case, and it reached a maximum value of $(T_{13} - T_{70}) = 150°\text{F}$ at approximately $t = 83$ sec. into the flight profile.

Figure 11 shows the time histories of nodal temperatures $\{T_{53}(t), T_{74}(t)\}$ at nodes {53, 74} of the middle spar lower welded site (fig. 4) for the two cases of contact conditions. Although the nodal temperature difference $(T_{53} - T_{74})$ at the lower weld site is less severe than $(T_{13} - T_{70})$ of the upper weld site, it is still substantial. For the partial contact case, the lower welded site nodal temperature difference $(T_{53} - T_{74})$ reached a maximum value of $(T_{53} - T_{74}) = 130$ °F at approximately $t = 123$ sec into the flight profile.

Shown in figure 12 are temperature time histories at locations down the middle spar and along the upper skin panel. The temperature gradient along the skin panel (between capacitor 13 and 14) appears to be greater than the temperature gradient from capacitor 13 to 70, but the distance between the two capacitors is longer. The temperature gradient per inch between capacitor 13 and 70 is actually larger. Temperature time histories on the upper skin panel can be seen in figure 13. The temperature gradient between capacitor 13 and 15 is higher than the gradients between capacitors 13 and 17 or 13 and 19. Distance between capacitors 13 and 15, 15 and 17, and 17 and 19 is 0.5 inches apart. Figure 14 shows nodal temperature time histories for node 7 of bay 1 upper skin and node 46 of bay 1 lower skin. Note that $\Delta T = T_7 - T_{46}$ reached a maximum value, $\Delta T = 546$ °F at $t = 89$ sec. As can be seen in the next figure, node 7 and node 46 are respectively the peak temperatures of the upper and lower skins.

Figure 15 shows the chord-wise distributions of the upper and lower skin temperatures at $t = 89$ sec into the flight profile. These temperature distributions were calculated from the thermal model with partial contact at the spar and skin weld sites. As can be seen from figure 15, the temperature distributions are steepest near the spars (heat sinks). Note that the panel temperature distribution over each bay is arch-shaped. This is the typical behavior of hot structural panels supported by the boundary heat sinks. The structural temperatures at typical points of the wing segment at $t = 89$ sec are listed in Table 4. The upper and lower wing skin temperatures listed are the peak temperatures of each bay.

Table 4. Structural temperatures at typical points of wing segment; $t = 89$ sec, °F

	Fore weld site	Bay 1 skin (peak)	Middle weld site	Bay 2 skin (peak)	Aft weld site
Upper	675	1,153	748	1,127	638
Lower	479	607	476	592	418

Notice that the designed flight trajectory caused the Hyper-X upper skin temperatures to be significantly higher than the lower skin temperatures. This implies that buckling is more critical for the upper wing panels than the lower wing panels. The panel temperature distributions of figure 15 and the

associated spar temperatures (not shown) were used as temperature inputs to the structural model for thermal stress and thermal buckling analyses of the wing segment.

Thermal Stress Analysis

The calculated chord-wise thermal stresses σ_x induced in the wing-segment skins under free expansion (to simulate actual situation) are listed in Table 5.

Table 5. Chord-wise stresses σ_x in the wing-segment skins; free expansion, lb/in^2.

	Front bay	Rear bay
Upper skin	–64,900	–61,364
Lower skin	–37,419	–31,938

Because the chord-wise thermal expansion of the wing panels are restrained by the cooler wing frame (heat sink), both upper and lower wing panels of each bay are under compression. Even though the temperature distribution over the wing panel of each bay is non-uniform and arch-shaped (fig. 15), the thermal stress induced in the wing panel of each bay is constant. This is the typical behavior of hot structural panels.

Figure 16 shows the deformed shape of the welded site under compression from wing panels of opposite bays, with element shear stresses indicated. The maximum shear stress τ_{max} is located at the aft upper corner element of the welded site (fig.16) with the value τ_{max} = 38,564 lb/in^2. The temperature at the middle spar upper welded site was calculated as T = 748°F at t = 89 sec. The shear failure stress τ_f at this temperature level is approximately $\tau_f \approx$ 54,000 lb/in^2 for Haynes 230 alloy. This value is one-half of the uniaxial tensile failure stress σ_f = 108,000 lb/in2 at T = 748°F based on Mohr's circle. Based on this current simple stress analysis, the maximum shear stress τ_{max} at the weld site will reach as high as 71 percent of the shear failure stress τ_f during Mach 7.5 heating.

Thermal Buckling Analysis

The results of thermal buckling analysis of the Hyper-X wing panels are presented in the following sections. On average, about 5~7 material iterations were required to obtain acceptable buckling solutions presented in these following sections.

Uniform Temperature Loading

Figures 17, 18, and 19, respectively, show the buckled shapes of the fore panel, aft panel and unit panel under uniform temperature loading and under different fixed support conditions. Note that, except for the SS-CL condition, the aft panel buckled at the unit panel region, and the buckled mode in this region (fig. 18) is similar to the buckled mode of the isolated unit panel (fig. 19). The buckling

temperatures calculated for those wing panel models subjected to uniform temperature loading are shown in Table 6.

Table 6. Buckling temperature of different wing-panel models under uniform temperature loading; fixed supports, $(T_u)_{cr}$, °F.

Support condition	Fore panel	Aft panel	Unit panel
SS-SS	167	121	97
SS-CL	176	188	239
CL-SS	355	175	114
CL-CL	410	294	295

The buckling temperatures listed in Table 6 are for the uniform temperature loading over the wing panel and not for the actual temperature loading. Because of the fixed boundary supports and fixed panel and stiffener joint site, the buckling temperatures are amazingly low. Note that, except at the SS-CL condition, the aft panel has lower buckling strength than the fore panel, and the buckling critical region is located at the unit panel region of the aft panel (fig.18).

In reality, the panel support sites (heat sinks) can expand when heated, resulting in the reduction of thermal stress levels in the wing panels as a result of reduced heat sink restraint. Therefore, the actual buckling temperatures could be much higher than the values presented in Table 6.

Dome-Shaped Temperature Loading

Figures 20 and 21 show, respectively, the buckled shapes of the wing segment under *actual* temperature loading (fig. 15) with fixed and free stiffeners. Note that the buckling mode of the wing segment is very similar to that of the fore panel with the CL-SS condition (fig. 17-c). The calculated buckling temperatures of the wing segment with fixed and free supports are shown in Table 7. The uniform temperature loading case is also included in that table for comparison.

Table 7. Buckling temperatures of wing segment panel under actual and uniform temperature loading.

	$(T_u)_{cr}$, °F	$(T_o)_{cr}$, °F	η
Uniform FX	260	-----	1.00
Actual FX	-----	389	1.50
Actual FR*	-----	1,324	5.09

* Closest to actual case

The wing segment model has only one row of E43 elements in the span-wise direction. Thus, the buckling solution termed "actual FR" in Table 7 may not be accurate enough to represent the buckling temperature of the two-dimensional wing panel. However, Table 7 can show how the "buckling temperature magnification factor of the first kind" η changes with the thermal loading and the boundary condition. Notice that the buckling temperature for the actual FR case is magnified by 5.09 times from the uniform FX case.

The unit panel was identified as the potential thermal buckling initiation zone based on the results of the uniform temperature loading buckling analysis (fig. 18 and Table 6). Therefore, thermal buckling analysis of the Hyper-X wing panels may be reduced to the thermal buckling analysis of the unit panel without going through complex modeling of the entire wing structure. Figures 22 and 23 show respectively the buckled shapes of the unit panel under dome-shaped temperature loading ($T_s/T_o = 0.54$, Hyper-X case) with fixed and free supports. For the fixed supports (fig. 22), the unit panel buckled into single half-waves in two different directions, one along the radial stiffeners and the other transverse to these radial stiffeners. But for the free support case (fig. 23), it buckled into two half-waves along the radial stiffeners. Table 8 shows buckling temperatures of the unit panel under dome-shaped temperature loading ($T_s/T_o = 0.54$, Hyper-X case) with different support conditions. The values of the η are also listed in the table. Data given in Table 6 for the uniform temperature loading case are also listed for comparison.

Table 8. Buckling temperatures of unit panel; $T_s/T_o = 0.54$ (Hyper-X case).

	Uniform FX		Dome-shaped FX		Dome-shaped FR	
Support	$(T_o)_{cr}$, °F	η	$(T_o)_{cr}$, °F	η	$(T_o)_{cr}$, °F	η
SS-SS	97	1.00	132	1.36	1.389*	14.32
SS-CL	239	1.00	357	1.49	2,290•	9.58
CL-SS	114	1.00	147	1.29	1,411	12.38
CL-CL	295	1.00	412	1.40	2,298•	7.79

* Closest to Hyper-X case

• Approaching melting range 2,375 °F ~ 2,500 °F of Haynes 230 alloy

Note that for the fixed supports, by changing the temperature loading from uniform to dome-shaped, the values of η are in the range of $1.29 \le \eta \le 1.49$ for all the support fixed conditions (low magnification in thermal buckling temperatures). However, for the dome-shaped temperature loading with free supports, the η values reached as high as $7.79 \le \eta \le 14.32$ range, implying a great magnification of buckling temperatures. The dome-shaped temperature loading with the SS-SS free support condition (closest to the Hyper-X case) has the highest η value ($\eta = 14.32$) and the CL-CL case has the lowest η value ($\eta = 7.79$). For the SS-CL and CL-CL cases, the buckling temperatures (indicated with solid dot in Table 7) approached the melting range 2,375°F ~ 2,500°F of the wing panel material. The buckling temperature 1,389 °F of the unit panel under the dome-shaped-free-SS-SS support condition (quite close to the buckling temperature 1,324 °F of the wing segment panel), could be a reasonable approximation to the

actual buckling temperature of the aft wing panel of the Hyper-X. The buckling temperature 1,389 °F of the unit panel is 1.20 times the calculated peak temperature 1,153 °F of the wing panels (fig.14). Thus, it is unlikely that the Hyper-X wing panels will buckle during the nominal Mach 7 flight trajectory.

Table 9 and10, respectively, show the buckling temperatures of unit panels under simply supported and clamped freely expandable boundaries subjected to dome-shaped temperature loading with different heat sink temperatures. The η and ξ are also listed.

Table 9. Buckling temperatures of unit panel under dome-shaped temperature loading; simply supported free boundaries.

T_s/T_o	0.	0.1	0.2	0.3	0.4	0.5	0.54*	0.6	0.7	0.8	0.9	1.0
$(T_o)_{cr}$, °F	826	872	971	1,067	1,189	1,352	1,389	1,458	1,732	2,507•	4,866•	∞
ξ	1.00	1.06	1.18	1.29	1.44	1.64	1.68	1.77	2.10	3.04	5.89	∞
η	8.52	8.99	10.01	11.00	12.26	13.97	14.32	15.03	17.86	25.85	50.16	∞

•Exceeded incipient melting point 2,345 °F of Haynes 230 alloy.
*Hyper-X

Table 10. Buckling temperatures of unit panel under dome-shaped temperature loading; clamped free boundaries.

T_s/T_o	0.	0.1	0.2	0.3	0.4	0.5	0.54*	0.6	0.7	0.8	0.9	1.0
$(T_o)_{cr}$, °F	1,294	1,385	1,408	1525	1661	1,857	1,942	2,141	2,763•	4,333•	8,447•	∞
ξ	1.00	1.07	1.09	1.18	1.29	1.44	1.50	1.65	2.14	3.35	6.53	∞
η	4.39	4.69	4.77	5.17	5.63	6.29	6.58	7.26	9.37	14.69	28.63	∞

•Exceeded incipient melting point 2,345 °F of Haynes 230 alloy.
*Hyper-X

The solid dot symbols in both Tables 8 and 10 indicate that the buckling temperatures have exceeded the melting range 2,375 °F ~ 2,500 °F of the wing panel material. At $T_s/T_o = 1$ for which the dome-shaped temperature distribution degenerates into uniform (flat) temperature distribution, the buckling temperatures reached infinity, implying that thermal buckling does not occur. Note that at $T_s/T_o = 0$ in Tables 9 and 10 (no heat sink thermal expansion), the buckling temperatures $\{(T_o)_{cr} = 826$ °F, $(T_o)_{cr} = 1{,}294$ °F$\}$ for the free simply supported and free clamped cases are much higher than the corresponding buckling temperatures $\{(T_o)_{cr} = 132$ °F, $(T_o)_{cr} = 412$ °F$\}$ for the fixed support cases (Table 8). This results from the fact that for the free support cases, the unheated heat sink still can deform elastically because of the thermal expansion of the unit panel, causing the buckling temperatures to be much higher.

For the simply supported case (Table 9), η is related to ξ through

$$\eta = \frac{(T_o)_{cr}}{(T_u)_{cr}} = \frac{826}{97}\xi = 8.52\xi \tag{7}$$

And, for the clamped case (Table 10),η is related to ξ through

$$\eta = \frac{(T_o)_{cr}}{(T_u)_{cr}} = \frac{1294}{295}\xi = 4.39\xi \tag{8}$$

The simply supported case has the numerical coefficient for ξ roughly twice of that for the clamped case (right-hand sides of equations (7) and (8)).

The data shown in Tables 9 and 10 are plotted respectively in figures 24 and 25 for easy visualization of how the buckling magnification factors η and ξ increase with the increasing heat sink temperature T_s/T_o. The η curve for the clamped free boundary case lies much below that for the simply supported free boundary case (fig. 24). The ξ curves (fig. 25) for the simply supported and clamped free boundary cases are quite close (Tables 9, 10). At $T_s/T_o = 1$, the dome-shaped temperature distribution degenerates into uniform temperature distribution, and the buckling temperatures reach infinity (i.e., no buckling). Both figures 24 and 25 are very useful for finding the value of η or ξ associated with heat sink temperature T_s/T_o at certain time steps after the launching.

CONCLUSIONS

Heat transfer, thermal stress, and thermal buckling analyses were performed on the Hyper-X wing structure for the Mach 7 mission. The key results of the analyses follow.

1. The maximum temperature differential between the upper and lower skins of the Hyper-X wing occurs at 89 sec after air launching from the B-52 aircraft. The profile of temperature distribution over the wing panel of each bay is dome-shaped.
2. The maximum shear stress τ_{max} at the welded site is estimated as τ_{max} = 38,564 lb/in^2, and is about 71 percent of the shear failure stress of the welding material.
3. By identifying the unit panel region as the potential thermal buckling initiation zone, thermal buckling analysis of the Hyper-X wing panels may be reduced to the thermal buckling analysis of the unit panel without going through complex modeling of the entire wing structure.
4. The estimated buckling temperature of the unit panel is $(T_o)_{cr}$ = 1,389 °F which is 1.20 times higher than the peak temperature 1,153 °F experienced by the wing panels under Mach 7.5 heating. This unit panel buckling solution may be considered as a reasonable estimate for the buckling temperature of the Hyper-X wing panels. This result suggests that Hyper-X wing panels are unlikely to buckle during a Mach 7 mission.
5. "Buckling temperature magnification factor of the first kind" η was established to scale up the panel buckling temperature in the uniform temperature loading case to estimate the panel buckling temperature of the dome-shaped temperature loading case.

6. "Buckling temperature magnification factor of the second kind" ξ was established to scale up the panel buckling temperature in the dome-shaped temperature loading case with unheated boundary heat sinks to generate a solution for the same case when boundary heat sinks are heated.

Dryden Flight Research Center
National Aeronautics and Space Administration
Edwards, California, April 12, 2001

APPENDIX

The temperature-dependent physical properties of Haynes 230 used for input to the thermal and structural models are listed in the following tables (Haynes International, Inc., Kokomo, Indiana).

Table A-1. Thermal properties of Haynes 230.

T, °F	c_p, Btu/lb °F	k, Btu/hr-ft °F	ε
70	0.095	5.167	0.85
200	0.099	5.917	0.85
400	0.104	7.250	0.85
600	0.108	8.500	0.85
800	0.112	9.833	0.85
1000	0.112	11.083	0.85
1200	0.134	12.333	0.85
1400	0.140	13.667	0.85
1600	0.145	14.917.	0.85
1800	0.147	16.250	0.85

Table A-2. Material properties of Haynes 230; $\rho = 0.324$ lb/in^3.

T, °F	$E \times 10^6$,lb/in^2	$\sigma_T \times 10^3$, lb/in^2	$\sigma_Y \times 10^3$, lb/in^2	$\alpha \times 10^{-6}$, in/in-°F	ν^*
70	30.6	125.4	57.4	7.0	0.310
200	30.1	(122.2)	(55.0)	7.1	0.311
400	29.3	(117.3)	(51.3)	7.2	0.315
600	28.3	(112.3)	(47.7)	7.4	0.318
800	27.3	(107.4)	(44.0)	7.6	0.321
1000	26.4	102.5	40.3	7.9	0.324
1200	25.3	97.7	39.5	8.1	0.330
1400	24.1	87.7	42.5	8.3	0.332
1600	23.1	63.1	37.3	8.6	0.334
1800	21.9	35.2	21.1	8.9	0.340
2000	20.7*	19.5	10.8	9.2*	0.343

* Estimated; ()Interpolated

REFERENCES

1. Ko, William L., Robert D. Quinn, and Leslie Gong, *Finite-Element Reentry Heat Transfer Analysis of Space Shuttle Orbiter*, NASA Technical Paper 2657, December 1986.

2. Ko, William L. and Raymond H. Jackson, *Compressive Buckling Analysis of Hat-Stiffened Panel*, NASA TM-4310, August 1991.

3. Ko, William L. and Raymond H. Jackson, *Shear Buckling Analysis of Hat-Stiffened Panel*, NASA TM-4644, November 1994.

4. Ko, William L. and Raymond H. Jackson, *Thermal Behavior of a Titanium Honeycomb-Core Sandwich Panel*, NASA TM-101732, January 1991.

5. Ko, William L. and Raymond H. Jackson, *Combined Compressive and Shear Buckling Analysis of Hypersonic Aircraft Structural Sandwich Panels*, NASA TM-4290, May 1991. Also published as AIAA Paper No. 92-2487-CP, in the proceedings of the 33rd AIAA/ASME/ASCE/AHS/ASC Structures, Structural Dynamics and Materials Conference, Dallas, Texas, April 13-15, 1992

6. Ko, William L., "Mechanical and Thermal Buckling Analysis of Sandwich Panels Under Different Edge Conditions," *Pacific International Conference on Aerospace Science and Technology Conference Proceedings*, *Vol. II*, Tainan, Taiwan, December 6-9, 1993.

7. Ko, William L., *Mechanical and Thermal Buckling Analysis of Rectangular Sandwich Panels under Different Edge Conditions*, NASA TM-4585, April 1994.

8. Ko, William L., *Prediction of Thermal Buckling Strengths of Hypersonic Aircraft Sandwich Panels Using Minimum Potential Energy and Finite Element Methods*, NASA TM-4643, May 1995.

9. Ko, William L. and Raymond H. Jackson, *Combined-Load Buckling Behavior of Metal-Matrix Composite Sandwich Panels Under Different Thermal Environments*, NASA TM-4321, September 1991.

10. Ko, William L. and Raymond H. Jackson, *Compressive and Shear Buckling Analysis of Metal Matrix Composite Sandwich Panels under Different Thermal Environments*, NASA TM-4492, June 1993. Also presented in *Composite Structures*, Vol. 25, July 1993, pp. 227-239.

11. Ko, William L., *Thermostructural Behavior of a Hypersonic Aircraft Sandwich Panel Subjected to Heating on One Side*, NASA TM-4769, April 1997.

12. Whetstone, W. D., *SPAR Structural Analysis System Reference Manual, System Level 13A*,Vol. 1, Program Execution, NASA CR-158970-1, December 1978.

13. Moeckel, W. E., *Oblique-Shock Relations at Hypersonic Speeds for Air in Chemical Equilibrium, NACA TN-3895*, January 1957.

14. Eckert, Ernst R. G., Survey of Boundary Layer Heat Transfer at High Velocities and High Temperatures, *WADC TR-59-624*, Wright-Patterson AFB, Ohio, April 1960.

15. Zoby, E. V., Moss, J. N., and Sutton, K., "Approximate Convective-Heating Equations for Hypersonic Flows," *J. Spacecraft and Rockets*, vol. 18, no. 1, Jan./Feb. 1981, pp. 64-70.

16. Hansen, C., Frederick, *Approximations for the Thermodynamic and Transport Properties of High-Temperature Air, NASA TR R-50, 1959.*

17. Ko, William L., *Mechanical- and Thermal-Buckling Behavior of Rectangular Plates With Different Central Cutouts*, NASA/TM-1998-206542, March 1998.

18. Richards, W. Lance and Randolph C. Thompson, *Titanium Honeycomb Panel Testing*. NASA TM-4768, October 1996. Also presented at Structural Testing Technology at High Temperature Conference, Dayton, Ohio, Nov. 4–6, 1991.

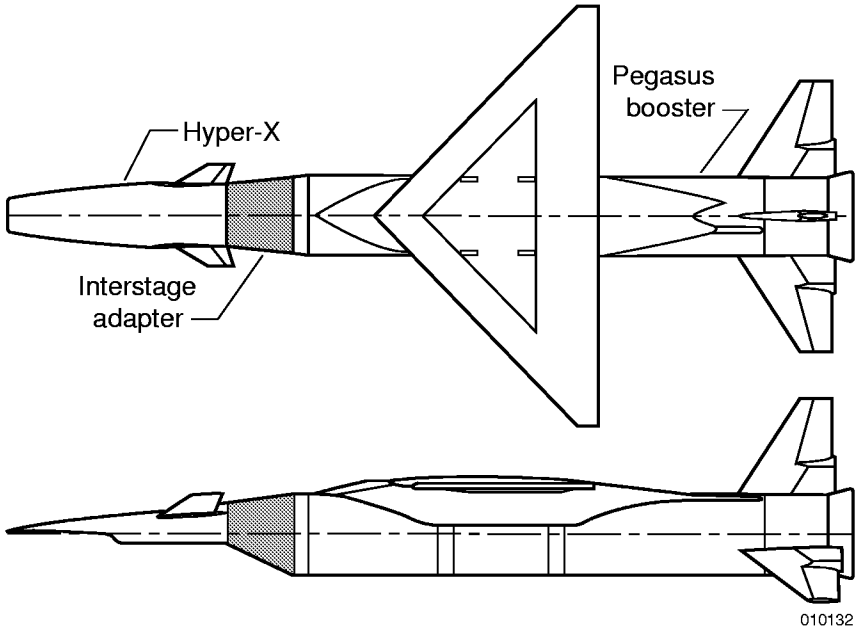

Figure 1. Hyper-X hypersonic flight research vehicle mated to the launch vehicle Pegasus® booster rocket.

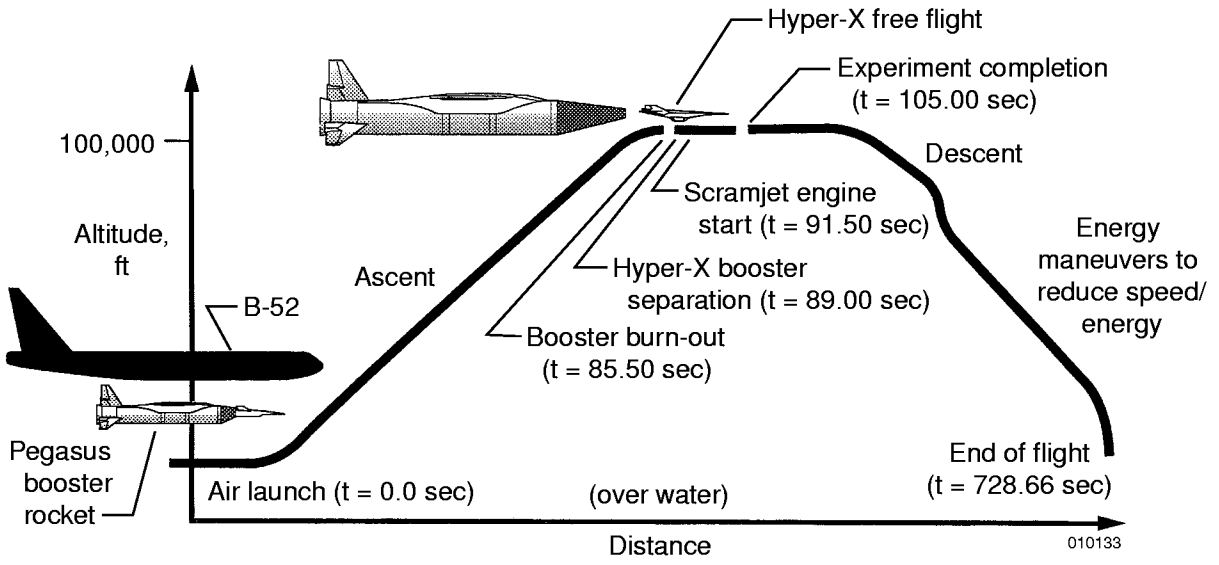

Figure 2. Hyper-X hypersonic flight research vehicle flight trajectory.

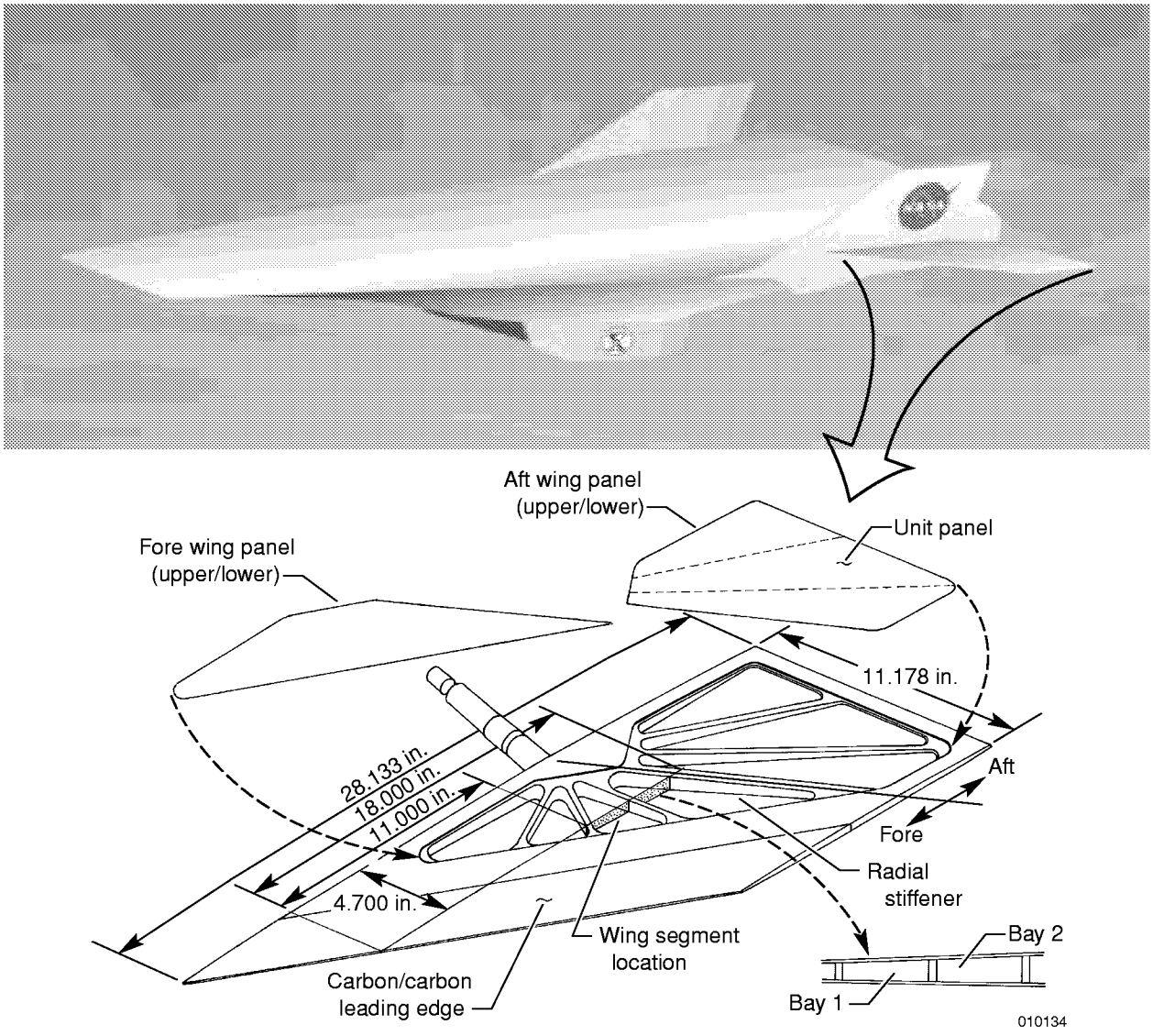

Figure 3. Unconventional wing structures of Hyper-X hypersonic flight research vehicle.

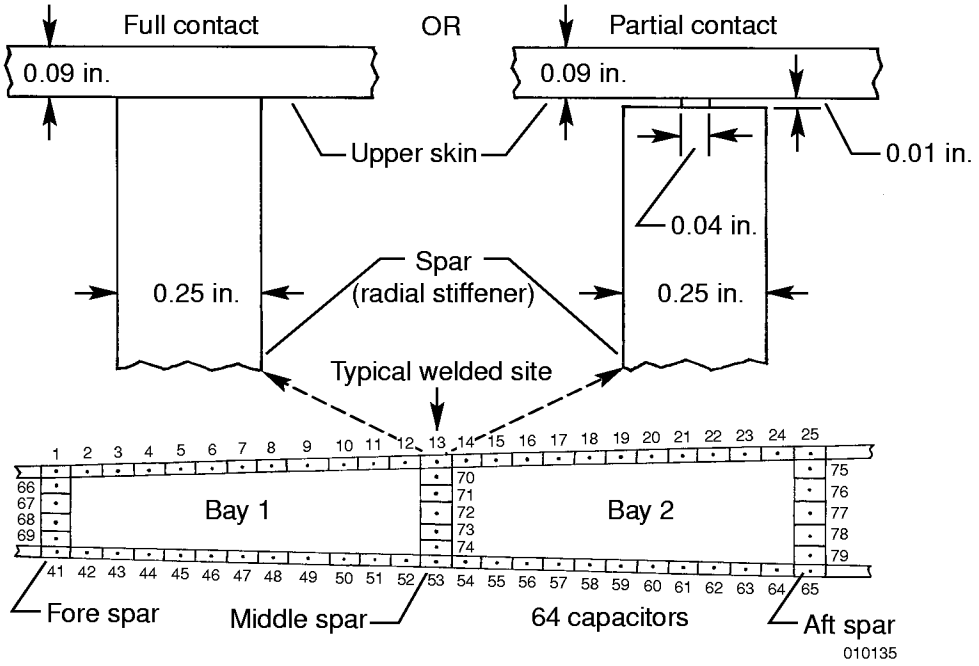

Figure 4. Finite-difference thermal model for Hyper-X wing segment; welded site dimensions in inches, full contact and partial contact.

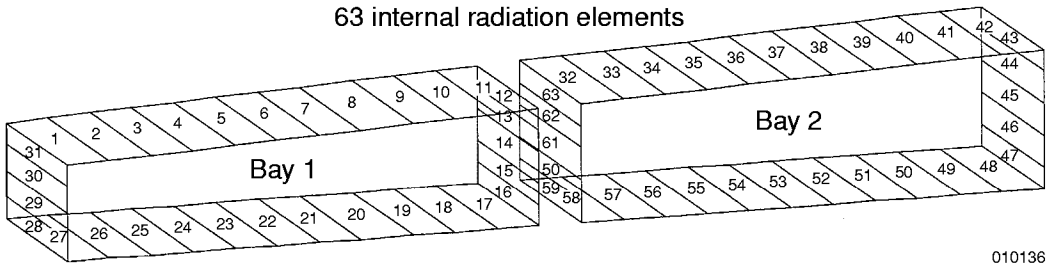

(a) Combined case.

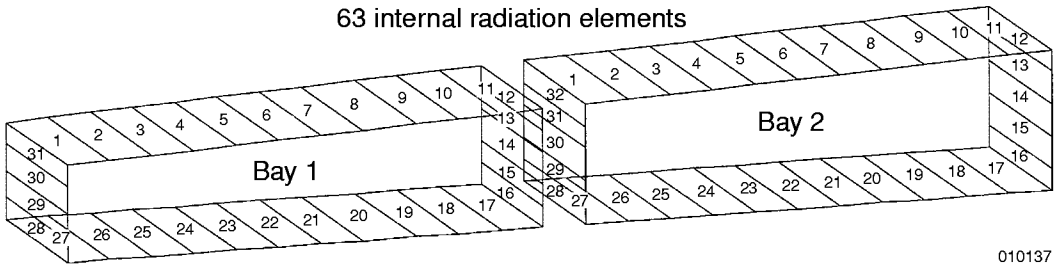

(b) Separate case.

Figure 5. SPAR finite-element models for computations of internal radiation view factors.

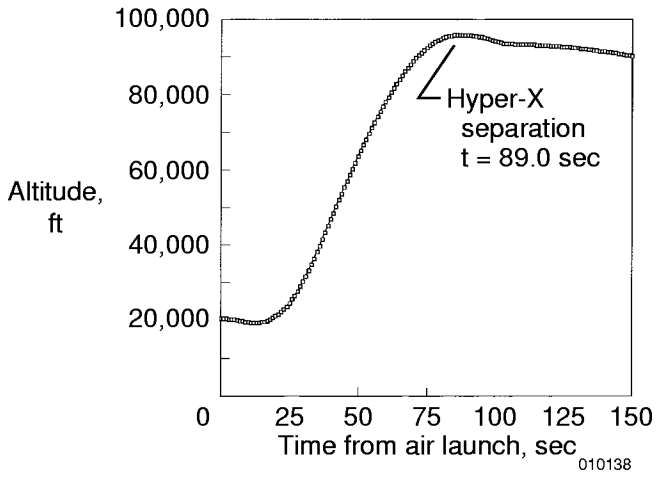

(a) Altitude.

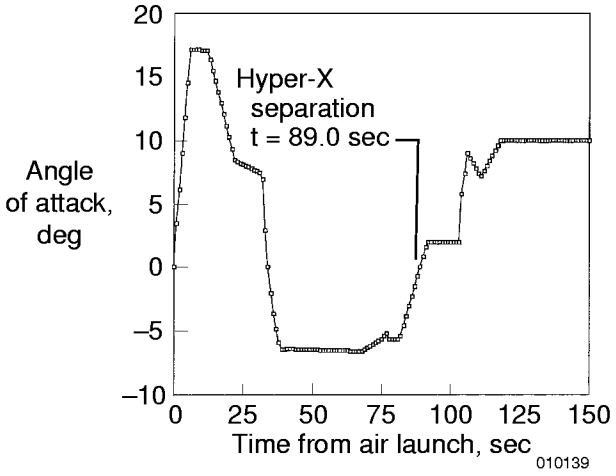

(b) Angle of attack.

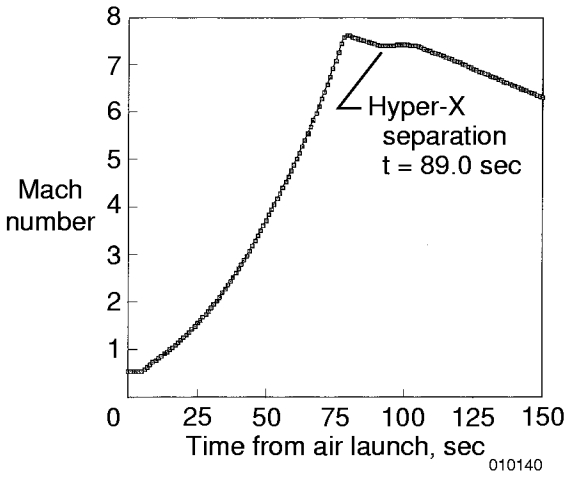

(c) Mach number.

Figure 6. Nominal Mach 7 mission flight trajectory of the Pegasus booster rocket carrying the Hyper-X vehicle for heating calculations.

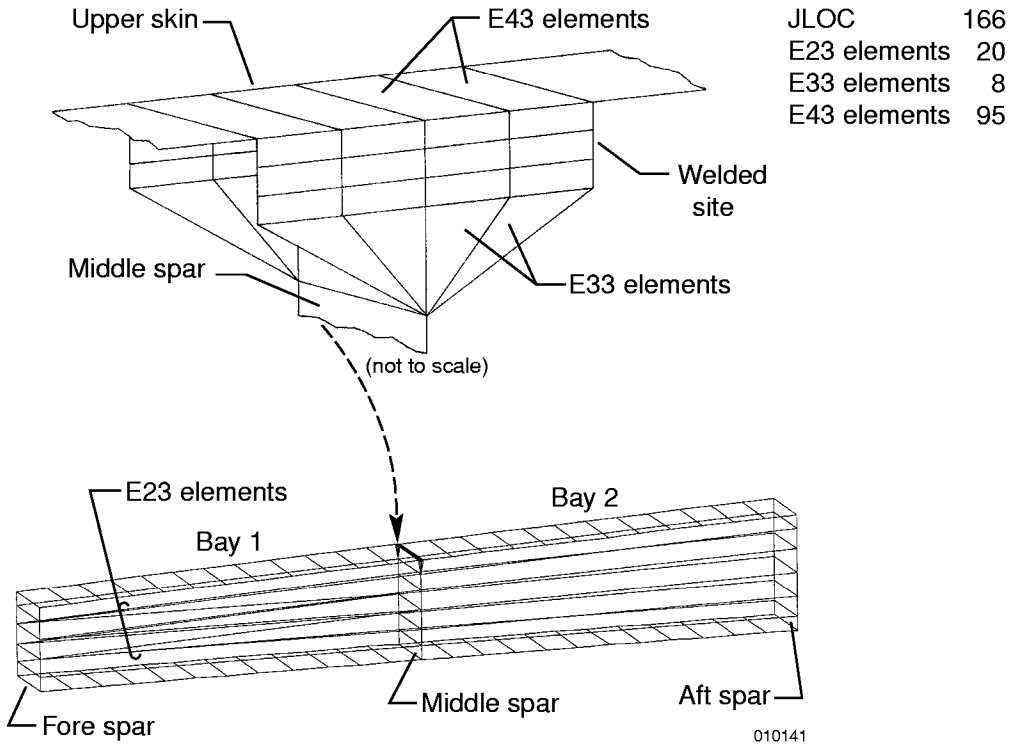

Figure 7. SPAR finite-element structural model for Hyper-X wing segment.

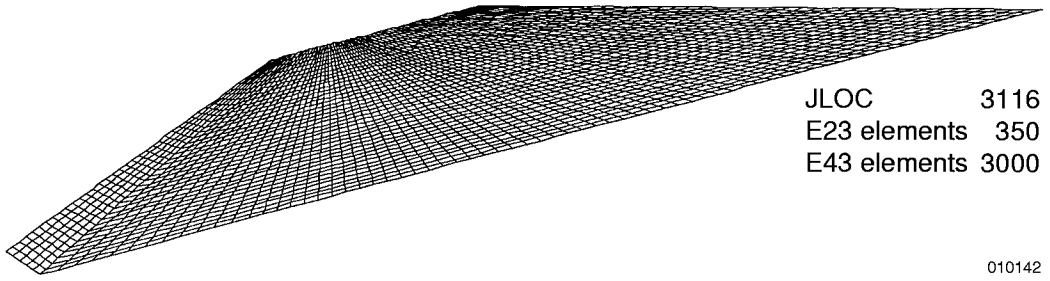

(a) Fore panel model.

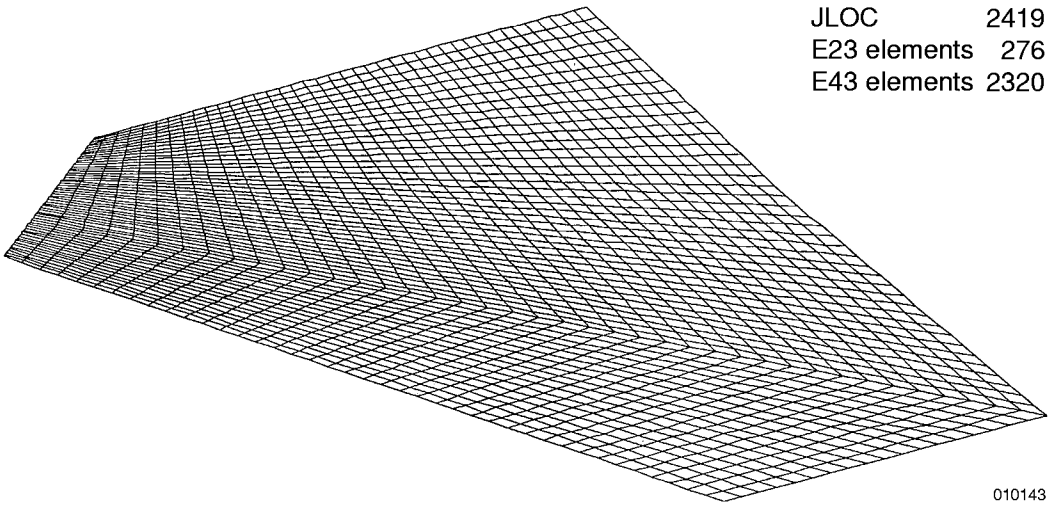

(b) Aft panel model.

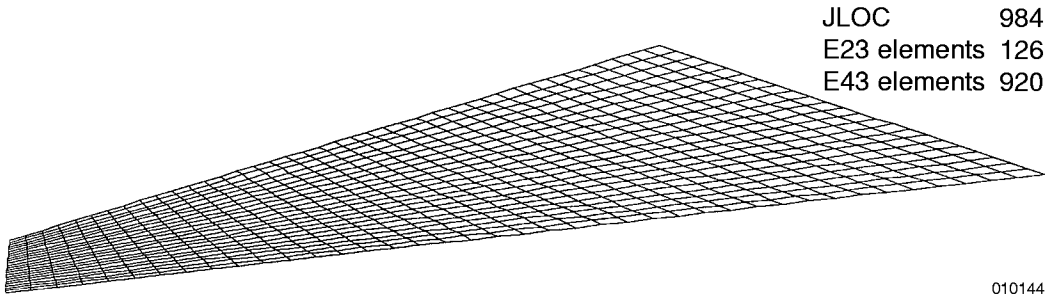

(c) Unit panel model

Figure 8. Three types of finite-element models for Hyper-X wing skins.

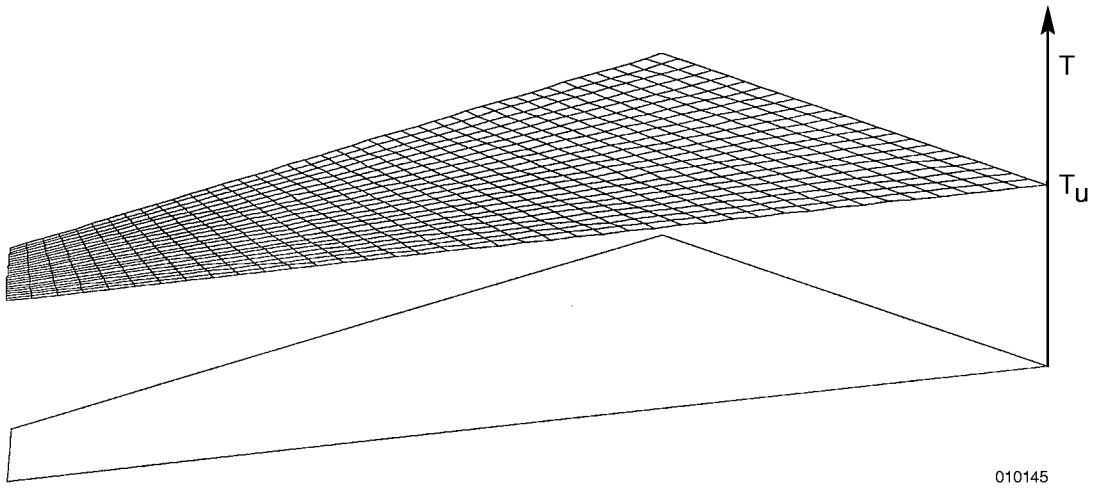

(a) Uniform temperature loading.

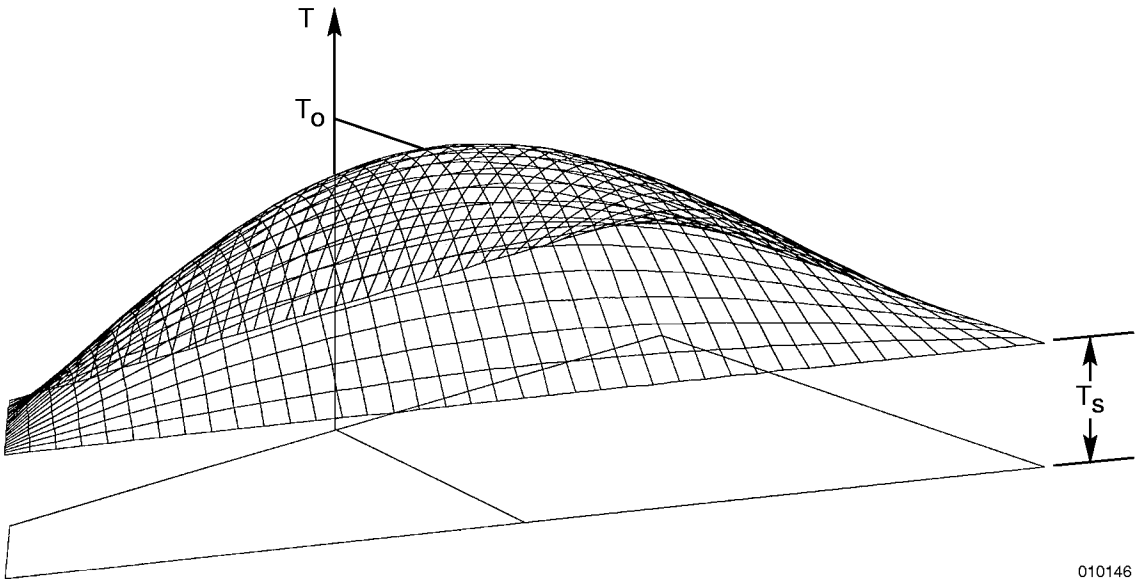

(b) Dome-shaped temperature loading.

Figure 9. Two types of temperature loading for the Hyper-X wing unit panel.

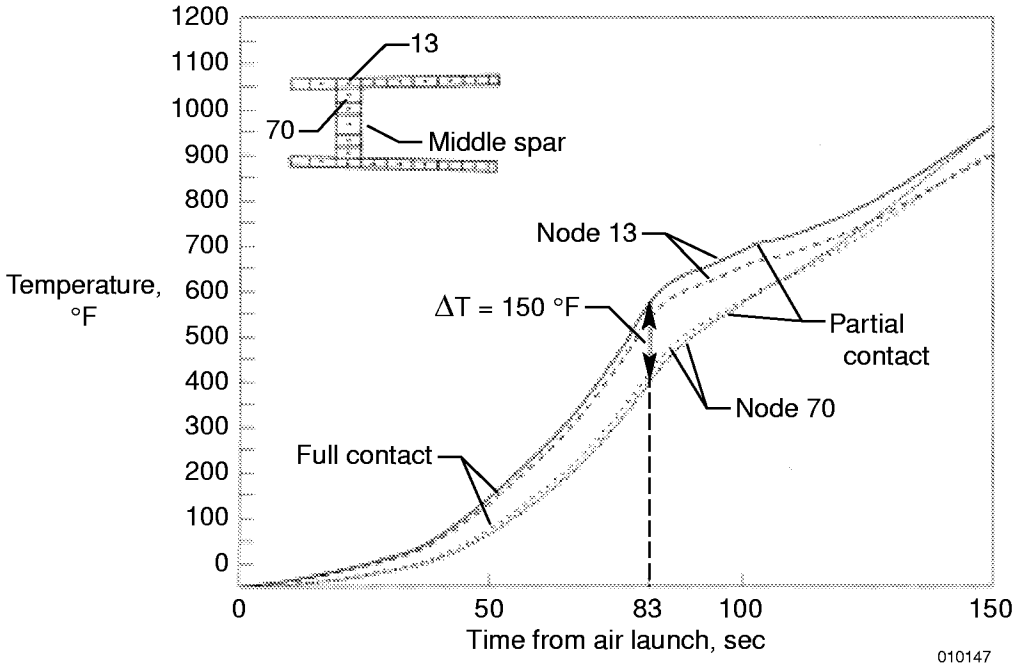

Figure 10. Nodal temperature time histories at the middle spar upper welded site; nodes 13, 70.

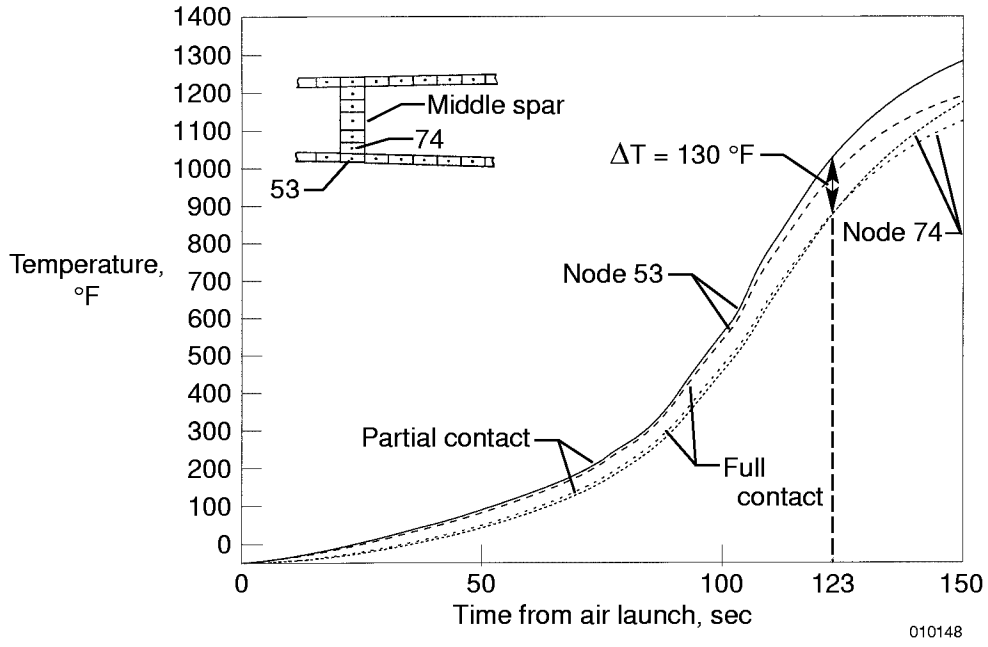

Figure 11. Nodal temperature time histories at the middle spar lower welded site; nodes 53, 74.

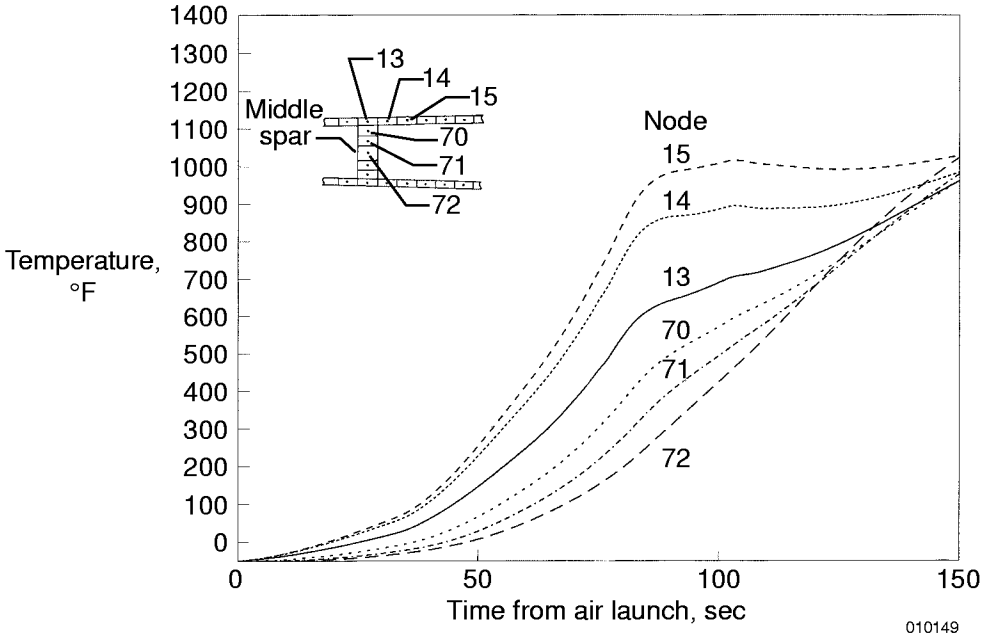

Figure 12. Nodal temperature time histories in the vicinity of the middle spar upper welded site.

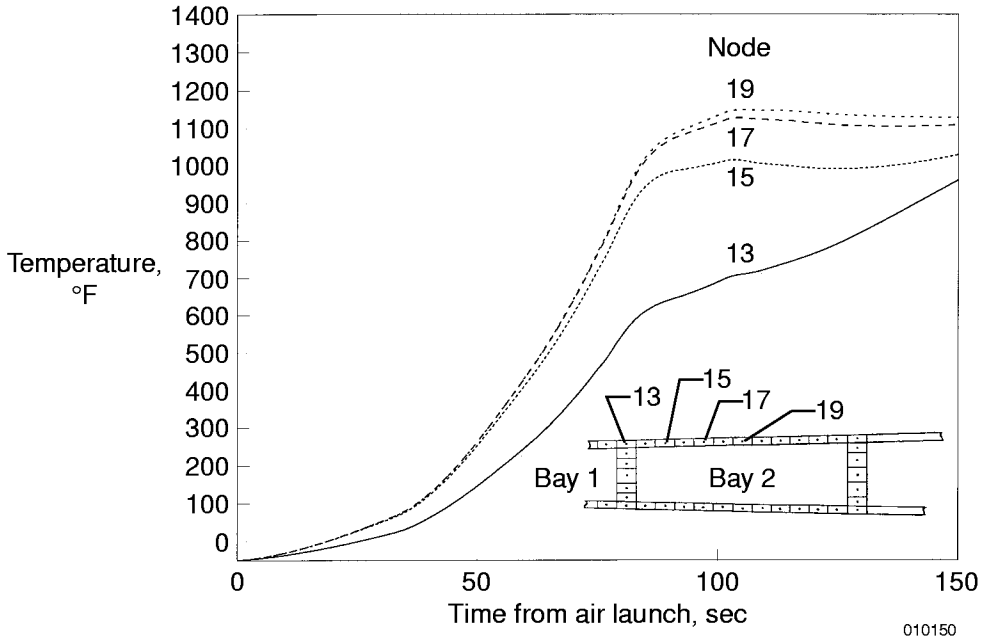

Figure 13. Upper skin nodal temperature time histories near the middle spar upper welded site.

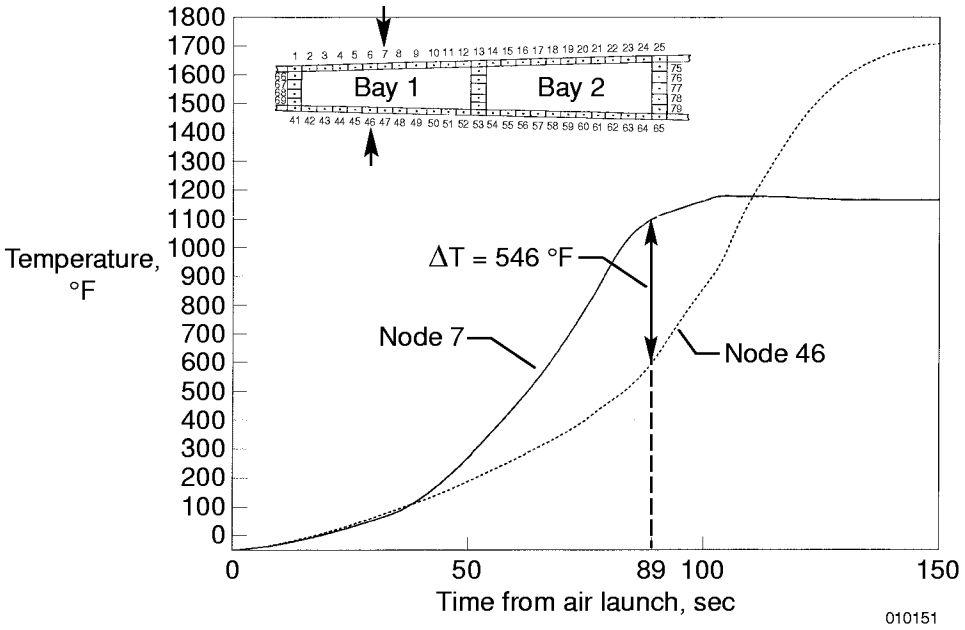

Figure 14. Nodal temperature time histories for node 7 of bay 1 upper skin and node 46 of bay 1 lower skin.

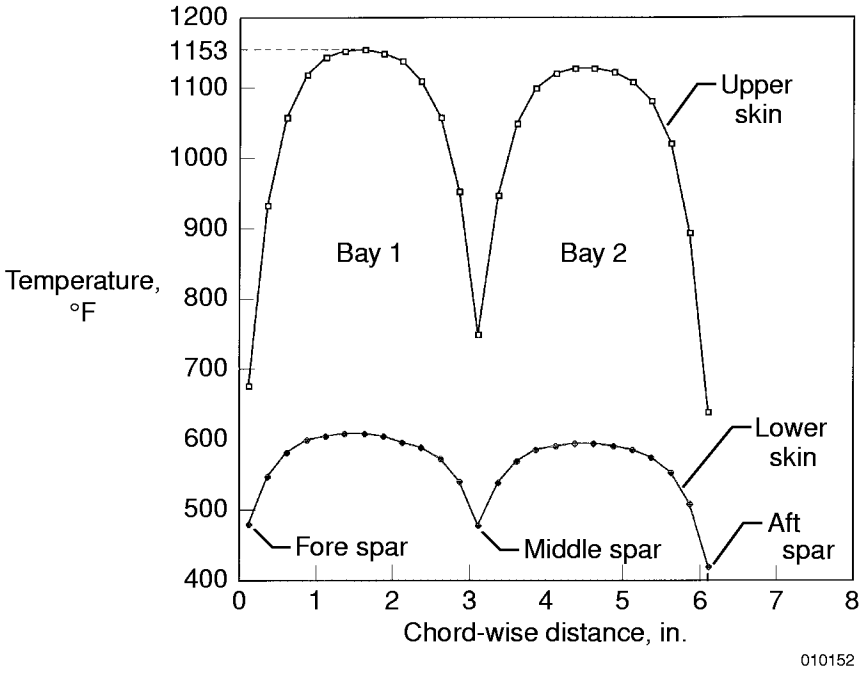

Figure 15. Chord-wise distributiuon of Hyper-X wing segment skin temperatures; t = 89 sec, 0.04 in. web contact.

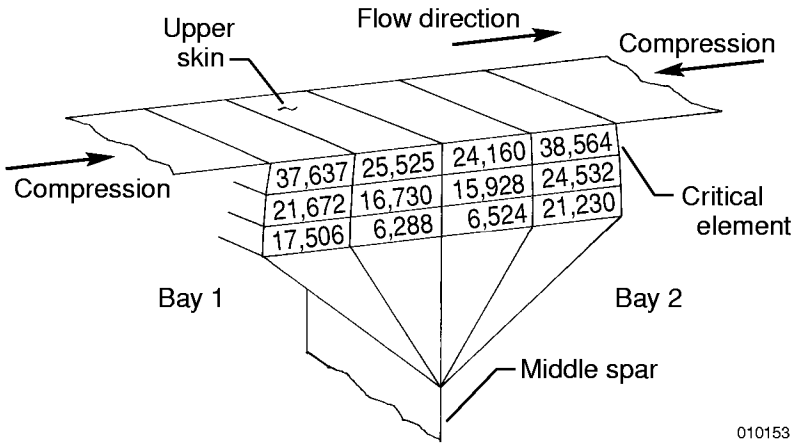

Figure 16. Deformed shape of welded site with element shear stresses indicated, lb/in^2; Mach 7.5 heating (nominal Mach 7 mission).

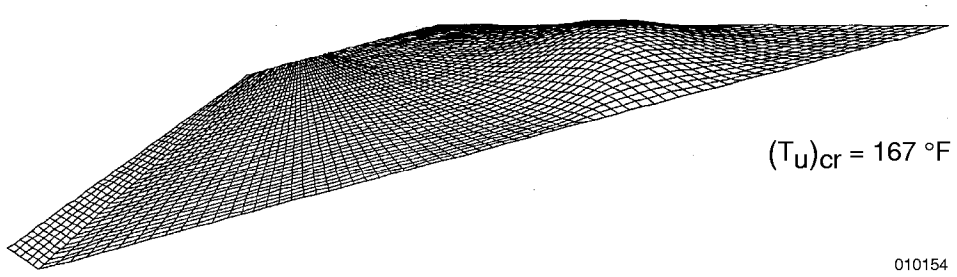

(a) SS-SS condition.

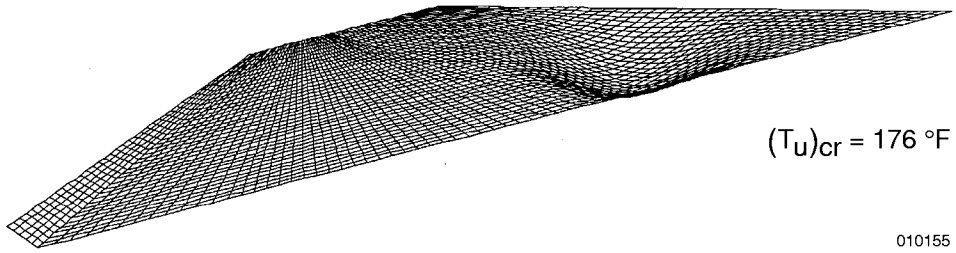

(b) SS-CL condition.

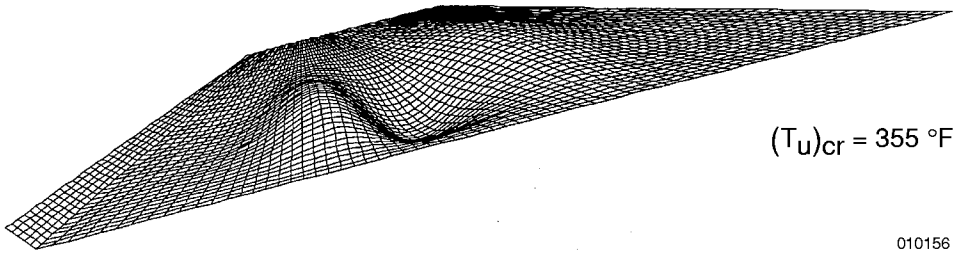

(c) CL-SS condition.

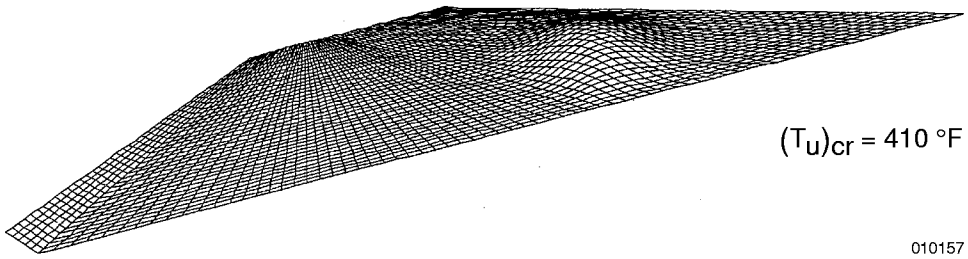

(d) CL-CL condition.

Figure 17. Buckled shapes of fore panel under different fixed support conditions, uniform temperature loading.

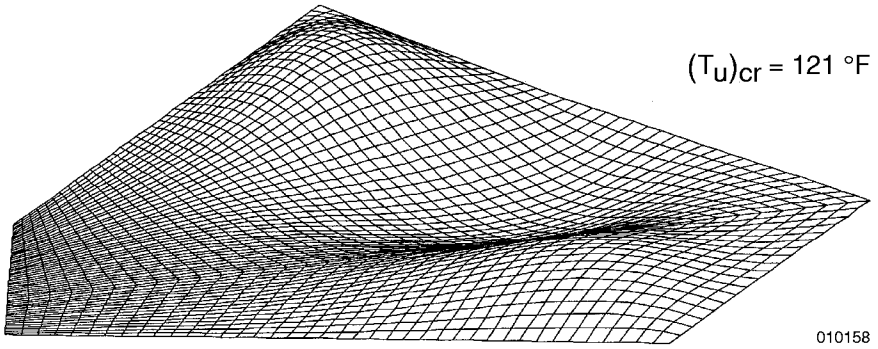

(a) SS-SS condition.

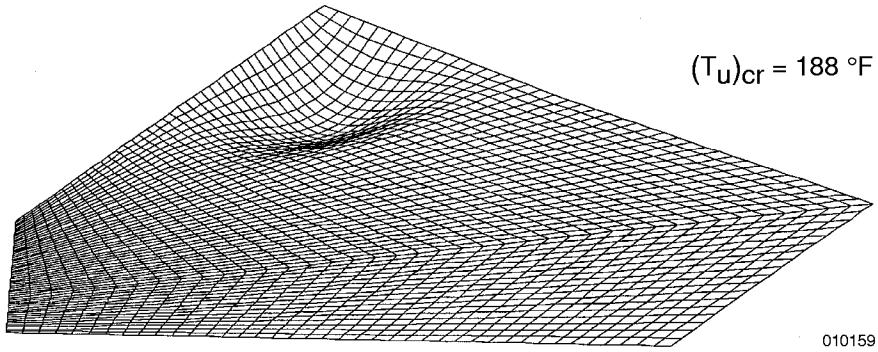

(b) SS-CL condition.

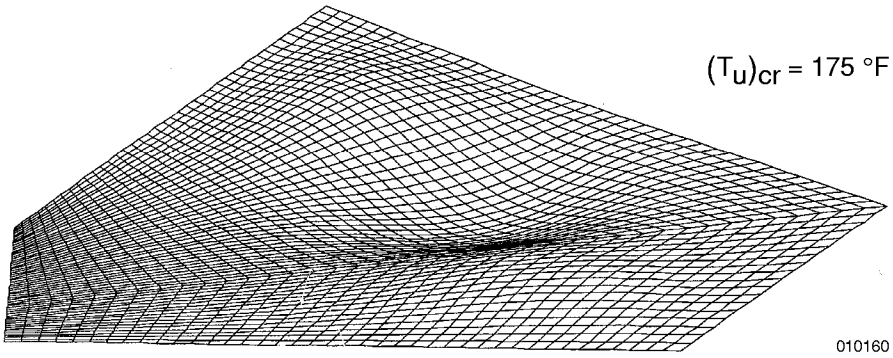

(c) CL-SS condition.

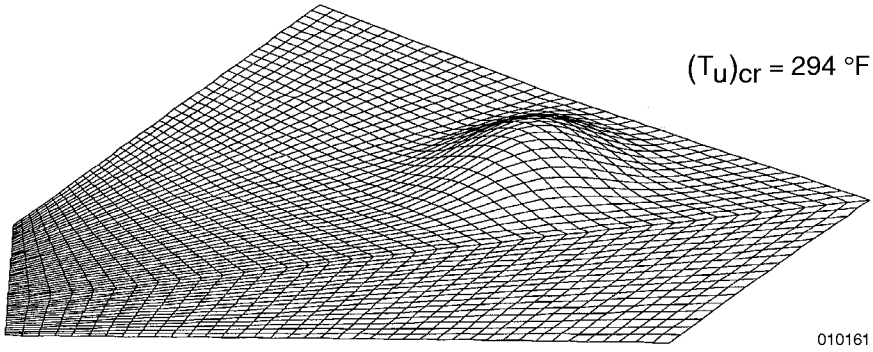

(d) CL-CL condition.

Figure 18. Buckled shapes of aft panel under different fixed support conditions, uniform temperature loading.

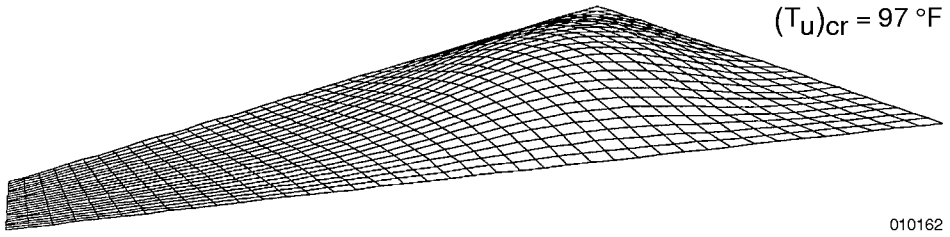

(a) SS-SS condition.

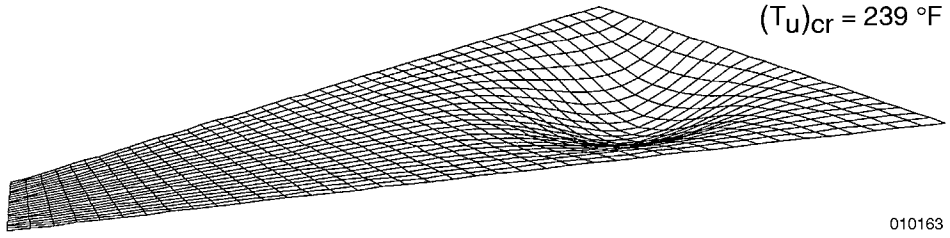

(b) SS-CL condition.

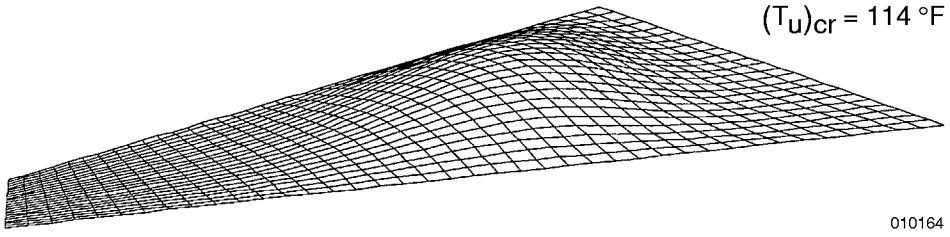

(c) CL-SS condition.

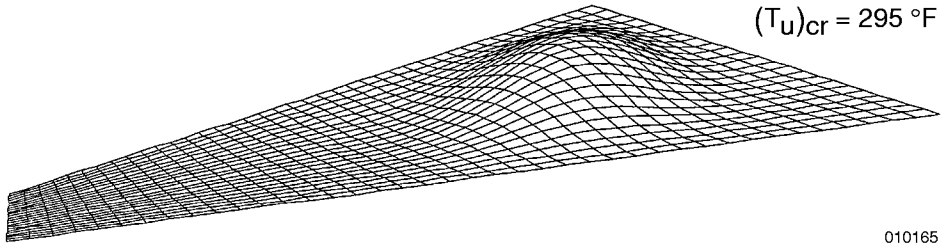

(d) CL-CL condition.

Figure 19. Buckled shapes of unit panel under different fixed support conditions, uniform temperature loading.

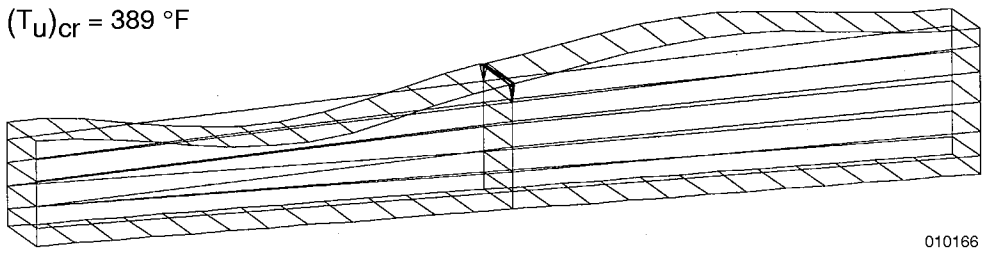

Figure 20. Buckled shape of wing segment under actual temperature loading at t = 89 sec, fixed stiffeners.

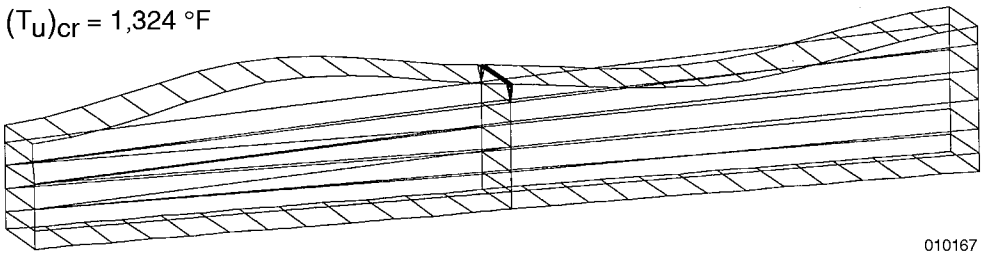

Figure 21. Buckled shape of wing segment under actual temperature loading at t = 89 sec, free stiffeners.

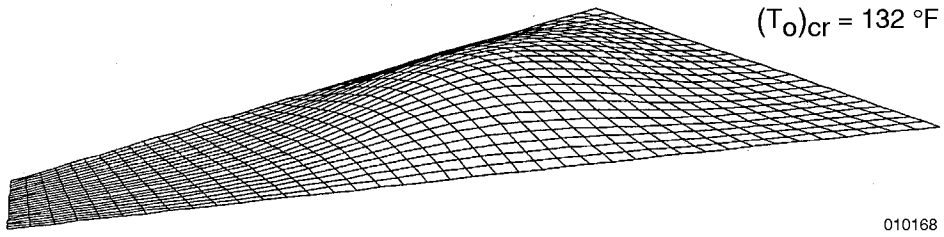

(a) SS-SS condition.

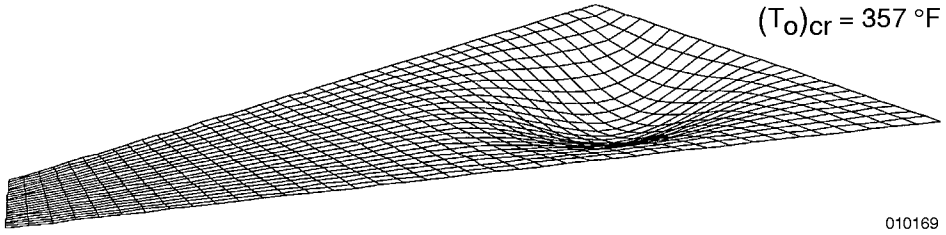

(b) SS-CL condition.

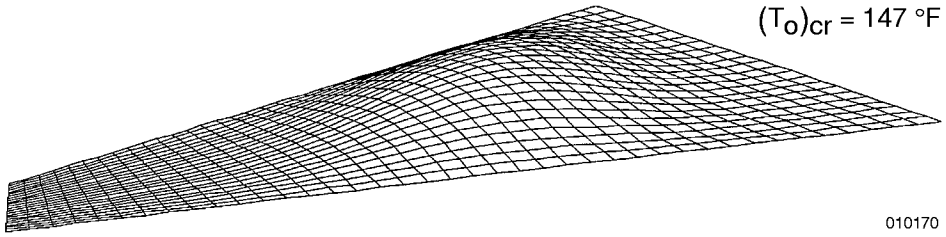

(c) CL-SS condition.

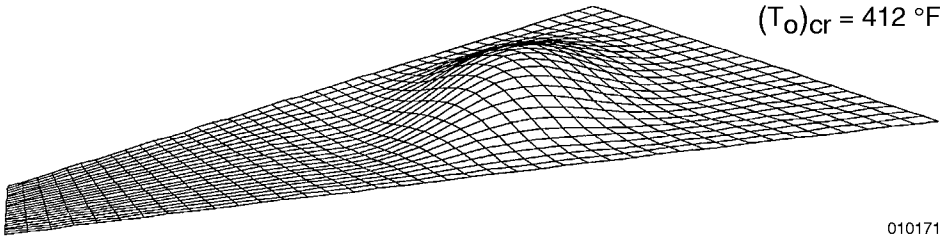

(d) CL-CL condition.

Figure 22. Buckled shapes of unit panel under different fixed support conditions, dome-shaped temperature loading, $T_s/T_o = 0.54$.

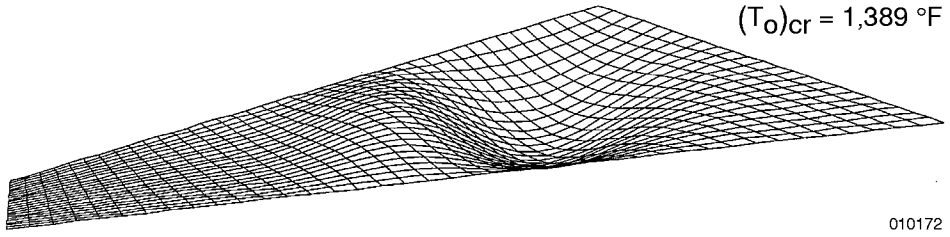

(a) SS-SS condition.

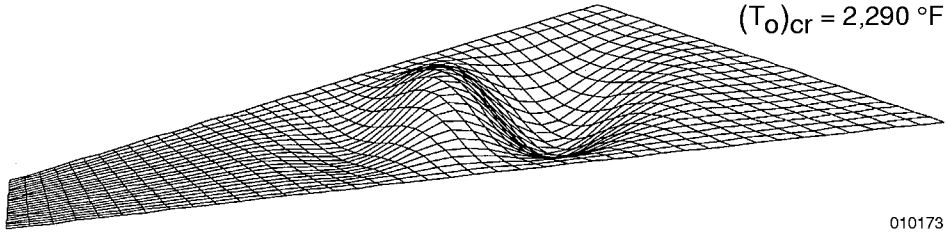

(b) SS-CL condition.

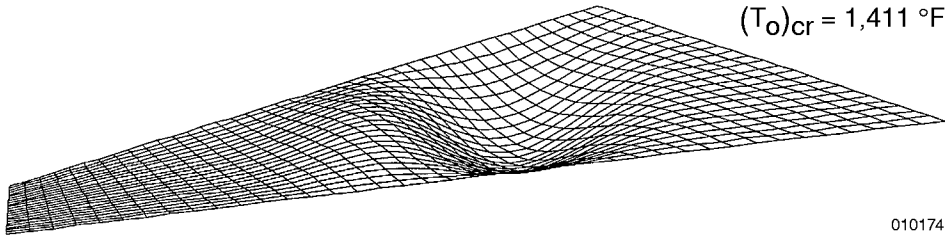

(c) CL-SS condition.

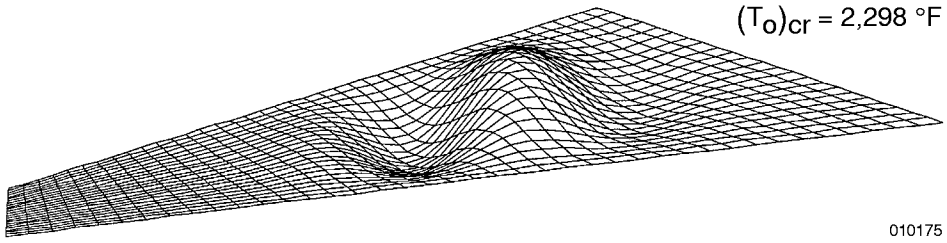

(d) CL-CL condition.

Figure 23. Buckled shapes of unit panel under different free support conditions, dome-shaped temperature loading, $T_s/T_o = 0.54$.

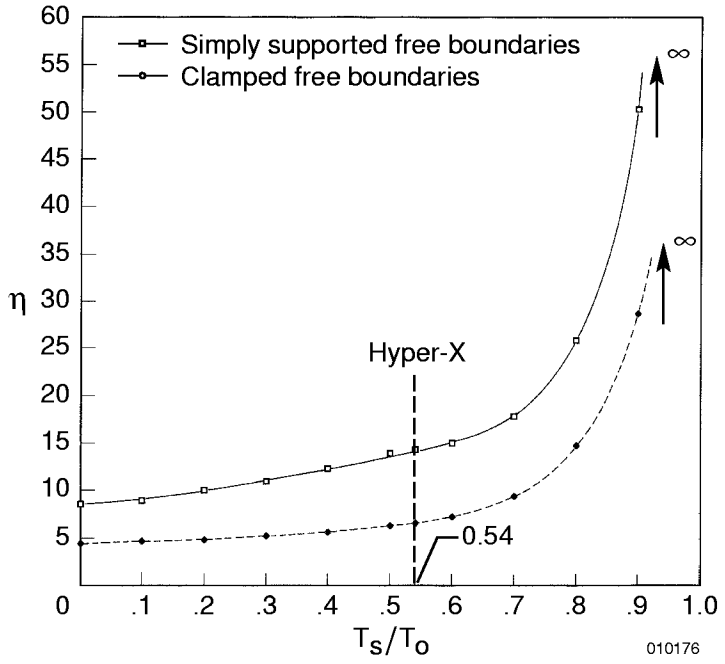

Figure 24. Plots of *buckling temperature magnification factors of the first kind*, η, as functions of boundary heat sink temperature T_s/T_o.

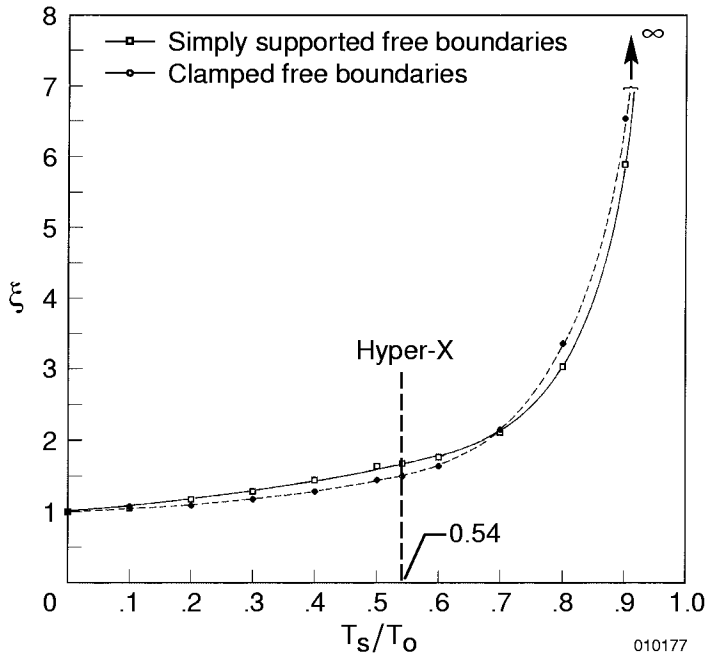

Figure 25. Plots of *buckling temperature magnification factors of the second kind*, ξ, as functions of boundary heat sink temperature T_s/T_o.

REPORT DOCUMENTATION PAGE

Form Approved
OMB No. 0704-0188

1. AGENCY USE ONLY (Leave blank)	2. REPORT DATE	3. REPORT TYPE AND DATES COVERED
	October 2001	Technical Publication

4. TITLE AND SUBTITLE

Thermostructural Analysis of Unconventional Wing Structures of a Hyper-X Hypersonic Flight Research Vehicle for the Mach 7 Mission

5. FUNDING NUMBERS

WU 710-55-24-E8-RR-00-000

6. AUTHOR(S)

William L. Ko and Leslie Gong

7. PERFORMING ORGANIZATION NAME(S) AND ADDRESS(ES)

NASA Dryden Flight Research Center
P.O. Box 273
Edwards, California 93523-0273

8. PERFORMING ORGANIZATION REPORT NUMBER

H-2453

9. SPONSORING/MONITORING AGENCY NAME(S) AND ADDRESS(ES)

National Aeronautics and Space Administration
Washington, DC 20546-0001

10. SPONSORING/MONITORING AGENCY REPORT NUMBER

NASA/TP-2001-210398

11. SUPPLEMENTARY NOTES

12a. DISTRIBUTION/AVAILABILITY STATEMENT

Unclassified—Unlimited
Subject Category 39

This report is available at http://www.dfrc.nasa.gov/DTRS/

12b. DISTRIBUTION CODE

13. ABSTRACT (Maximum 200 words)

Heat transfer, thermal stresses, and thermal buckling analyses were performed on the unconventional wing structures of a Hyper-X hypersonic flight research vehicle (designated as X-43) subjected to nominal Mach 7 aerodynamic heating. A wing midspan cross section was selected for the heat transfer and thermal stress analyses. Thermal buckling analysis was performed on three regions of the wing skin (lower or upper); 1) a fore wing panel, 2) an aft wing panel, and 3) a unit panel at the middle of the aft wing panel. A fourth thermal buckling analysis was performed on a midspan wing segment. The unit panel region is identified as the potential thermal buckling initiation zone. Therefore, thermal buckling analysis of the Hyper-X wing panels could be reduced to the thermal buckling analysis of that unit panel. "Buckling temperature magnification factors" were established. Structural temperature-time histories are presented. The results show that the concerns of shear failure at wing and spar welded sites, and of thermal buckling of Hyper-X wing panels, may not arise under Mach 7 conditions.

14. SUBJECT TERMS

Buckling temperature magnification factors, Hyper-X wing, Irregular panels, Non-uniform temperature loading, Thermal buckling

15. NUMBER OF PAGES

43

16. PRICE CODE

A03

17. SECURITY CLASSIFICATION OF REPORT	18. SECURITY CLASSIFICATION OF THIS PAGE	19. SECURITY CLASSIFICATION OF ABSTRACT	20. LIMITATION OF ABSTRACT
Unclassified	Unclassified	Unclassified	Unlimited